AIAA JOURNAL
Vol. 50, No. 2, February 2012

Eddy-Preserving Limiter for Unsteady Subsonic Flows

Kaveh Mohamed* and Siva Nadarajah†
McGill University, Montreal, Quebec H3A 2K6, Canada
and
Marius Paraschivoiu‡
Concordia University, Montreal, Quebec H3G 1M8, Canada

DOI: 10.2514/1.J051200

A slope-limiting algorithm for second-order monotone upstream-centered schemes for conservation laws is introduced to reduce the dissipation of vortices in flow simulations. The algorithm is based on the reconstruction of velocity components along the principle axes of the vortex and the augmentation of the central gradients' weight for the interpolation of velocity components on the swirl plane of the vortex. The performance of the scheme in different vortical flow problems is investigated. The proposed limiting algorithm has been able to considerably reduce the dissipation of vortices provided that the spatial and temporal discretization of the problem have been fine enough to resolve the length and time scales of the corresponding vortical motion. In particular, the scheme has significantly outperformed the conventional van Albada limiter to resolve the second peak in the lift coefficient spectra in the case of a NACA0021 airfoil at a poststall condition.

Nomenclature

C	=	control volume
C_{DES}	=	detached-eddy simulation coefficients
d	=	distance from the wall
$\tilde{d}$	=	modified distance from the wall
$\mathcal{F}$	=	Roe flux
$\mathbf{F}$	=	convective flux
f_d	=	delayed detached-eddy simulation function
h	=	helicity factor
κ	=	blending factor for slope calculation
$\mathbf{M}$	=	transformation matrix from Cartesian to vortex coordinate system
$\mathbf{n}$	=	radial vector toward the center on the swirl plane
p	=	pressure
$\mathbf{P}_c$	=	low-speed preconditioning matrix for conservative variables
$\mathbf{r}$	=	vector of position
$\mathcal{S}_\omega$	=	vortex coordinate system
$\mathcal{S}_0$	=	Cartesian coordinate system
$\mathbf{s}$	=	vector of the mesh edge
$\mathbf{U}$	=	vector of conservative variables
$\mathbf{u}_r$, $\mathbf{u}_{cr}$, and $\mathbf{u}_{ci}$	=	real eigenvector, real, and imaginary parts of complex eigenvector of velocity gradient tensor
$\mathbf{V}$	=	vector of primitive variables
$\mathbf{v}$	=	flow velocity vector
α	=	artificial dissipation scaledown factor
β, δ	=	thresholds to specify orbital compactness of vortical motion
$\mathbf{\Delta}$	=	vector of primitive variable increments
ϵ	=	small constant
ε	=	velocity component along vorticity vector
Φ	=	slope limiter
η_ω	=	helicity threshold
λ_r, λ_{cr}, and λ_{ci}	=	real eigenvalue, real, and imaginary parts of the complex eigenvalue of velocity gradient tensor
$\boldsymbol{\omega}$	=	vorticity vector
ρ	=	density
σ_ω	=	helicity sensor
$\boldsymbol{\tau}$	=	tangential velocity direction on swirl plane of a vortex
$\|\|$	=	L_2-norm
$'$	=	variables in vortex system
$\cdot$	=	dot product
$\hat{}$	=	normalized vector
$\bar{}$	=	averaged quantity
$\imath$	=	$\sqrt{-1}$
∇	=	gradient operator
∂C	=	control volume boundary surfaces

Subscripts

i, j	=	evaluated at grid point i, j
r, cr, ci	=	components along $\mathbf{u}_r$, $\mathbf{u}_{cr}$, $\mathbf{u}_{ci}$ vectors
x, y, z	=	x, y, z components of a vector in Cartesian system

Superscripts

-1	=	inverse
$+-$	=	left and right interpolated values
c	=	central component
T	=	transpose
u	=	upwind component

Received 16 February 2011; revision received 22 June 2011; accepted for publication 18 August 2011.

*Ph.D. Candidate, Department of Mechanical Engineering.
†Associate Professor, Department of Mechanical Engineering. Member AIAA.
‡Professor, Department of Mechanical and Industrial Engineering. Member AIAA.

I. Introduction

NUMERICAL modeling of the vortical flow is of great importance to many engineering fluid dynamic applications. Aerodynamic stability and control of aircraft are greatly influenced by vortical flow phenomena such as the vortex formation and its interaction with high-lift devices, particularly as a result of the installation of vortex generators [1] and vortex breakdowns [2,3]. Ship hydrodynamics, likewise, involves numerous vortical flow features that are crucial for the performance assessment of the vehicle [4]. Numerical algorithms capable of accurately capturing vortex characteristics and its interactions with the surrounding turbulent flowfield can hence provide valuable predictions to many engineering applications.

Two main factors compete to impede the resolution of vortices in Reynolds-averaged Navier Stokes (RANS) simulations: the artificial

dissipation of flux calculation schemes and the turbulence viscosity. By vortices, herein, we intend not only individual and statistically well-defined vortices such as tip-vortices or leading-edge separation vortices, but also stochastic turbulent eddies. Even though the spatial and the temporal discretizations of a simulation might be sufficiently fine to capture vortical motions of certain length scales, the resolution of vortices can be significantly impaired due to high artificial dissipation or excessive turbulent viscosity.

Several modifications have been proposed to reduce the level of turbulence viscosity in vortical regions of the flow. The production term in the majority of turbulence models is a function of local flow vorticity; hence in the core of a vortex, this term is overactivated and an excessive amount of turbulence viscosity is generated. Dacles–Mariani et al. [5] and Spalart and Shur [6] curvature introduced a sensor based on the ratio of the magnitude of the local strain tensor and the local vorticity to distinguish pure vortical regions of the flow from shear layers where both strain tensor and vorticity have considerable magnitudes. The production term of the turbulence viscosity in the Spalart–Allmaras (SA) equation is then reduced as a function of this sensor in the vortical flow regions. Brandsma et al. [7] proposed similar modifications for the k-ω turbulence model. In the detached eddy simulation (DES) [8] and the delayed detached eddy simulation (DDES) [9] schemes proposed by Spalart et al., the destruction term of the SA model is augmented outside the attached boundary layer where turbulent eddies resulting from flow separation are present. This reduces the level of the turbulence viscosity in the large eddy simulation (LES) region and hence improves the resolution of turbulent eddies. As the majority of test cases studied in this paper involve massive flow separation, we adopted the DDES method to reduce the turbulent viscosity level.

Popular second-order finite volume convective flux calculation schemes tend to exhibit overdissipative behavior in vortical flow regions. On the swirl plane of a vortex, it is quite likely that the velocity components reach to a local extremum value along any arbitrary direction due to the constant change of the flow direction. The artificial dissipation of the second-order schemes, on the other hand, significantly increases in the presence of local maxima or minima. This behavior is common both for upwind schemes including monotone upstream-centered schemes for conservation laws (MUSCL) and for their central counterparts such as Jameson–Schmidt–Turkel scalar- [10] and matrix-dissipation [11] schemes. Higher-order schemes can be considered as the ultimate remedy for this issue. However, with recent advances and validation for basic engineering cases [12,13], further developments are expected to improve the robustness of these schemes for industrial-strength cases involving complex configurations where grid quality is usually sacrificed to resolve the complexity of the geometry.

To alleviate the overdissipative behavior of second-order schemes in vortical regions of the flow, two approaches have been commonly used: vorticity confinement method and artificial dissipation scaledown. In the vorticity confinement method [14,15], a source term is added to the momentum equation. The direction of the source term is determined based on the principle axes of the vortex; i.e., a vorticity vector and a normal vector directed toward the vortex center. This approach is well suited to statistically well-defined vortices where the vortex and its principle axes experience no significant distortion during the simulation time. Turbulent eddies, on the other hand, can undergo huge deformations, are transient, and can have very short life spans. The common practice to preserve these eddies in DES problems is to reduce the artificial dissipation of the convective flux formulation. The dissipative or upwind contributions of fluxes corresponding to all flow variables are scaled down by a single scalar coefficient whose magnitude varies in the computational domain. Various expressions for the scaledown factor pertaining to several finite volume convective flux calculation schemes have been proposed [16–19]. A major challenge here is to limit the scaledown activated region as much as possible to the eddy dominated area (the focus region in the DES terminology [20]), as the further extension of the artificial dissipation reduction to the Euler region leads to the slower convergence of the flow solver.

Löhner [21] developed a new limiting algorithm alongside variable reconstruction MUSCL schemes to lower the artificial dissipation within a vortex structure. The basic idea is to prevent the activation of the slope limiter during the reconstruction of the velocity component in a certain direction along which, due to the vortical motion, an extremum occurs. The principle direction of the vortex is defined via the vorticity vector, a normal vector toward the vortex center, and a tangential vector defined as the outer product of the vorticity and the normal vectors. This definition, which implies the perpendicularity of the vortex axis and its swirl plane, lacks the generality, especially in the case of turbulent eddies undergoing stretching and bending. Furthermore, the vortical structures are recognized as flow regions where a helicity sensor exceeds a given threshold value. The existence of eddies with a wide range of strengths in the turbulent flow makes the definition of an appropriate threshold value ambiguous.

An eddy-preserving slope limiter is introduced in this paper to mitigate the overdissipation of vortices in second-order finite volume MUSCL variable reconstruction schemes. This work is inspired by the idea of the minimal vorticity dissipation limiters of Löhner [21]. A vortex-identification scheme based on the existence of complex eigenvalues for the velocity gradient tensor [22] is used to activate the proposed limiting algorithm in the computational domain. This makes the detection of vortical structures regardless of their strengths possible. Moreover, principle directions of eddies are determined based on eigenvectors of the velocity gradient, and no specific assumption regarding their relative orientation is made. The scheme dissipation is lowered during the velocity component reconstruction on the swirl plane of the vortex. This is achieved via inactivating the slope limiter as well as increasing the weight of central gradients used for interpolating velocity components on the swirl plane of the vortex. The vortex dissipation reduction is minor if only the reconstruction of the velocity components on the swirl plane of the vortex are performed while the slope limiter is kept inactive. The higher weight of central gradients improve the vortex resolution significantly further. Likewise in the Löhner's approach [21], the inactivation of the slope limiter is employed in conjunction with the vorticity confinement method. The higher central gradient approach, unlike the vorticity confinement method, is applicable to unsteady deforming eddies.

Low-speed vortical flows studied in this paper involve neither shock waves nor other discontinuities. However, due to the presence of vortices, the distribution of velocity components and static pressure throughout the computational domain experiences numerous extrema. The inactivation of the slope limiter during MUSCL variable reconstruction in vortical flow regions can lead to further dissipation of vortices as the upwind and central slopes with opposite signs can very likely result in a bigger jump between the left and right interpolated values as compared with the jump obtained via a zero slope interpolation.

The paper contains the following sections. Numerical schemes are explained in Sec. II. It includes a brief review of the implementation of the RANS and DES models, the conventional van Albada limiter, Löhner's minimal vorticity dissipation limiter, and the description of the proposed eddy-preserving limiting algorithm. The performance of various turbulence modeling and artificial dissipation reduction schemes are compared in Sec. III. The test cases studied include the decay of isotropic turbulence (DIT) in a periodic cube, the tip-vortex characteristics of a NACA0015 wing at high angle of attacks (AOAs), and unsteady aerodynamic forces around a NACA0021 airfoil at a static stall condition. The effectiveness of the eddy-preserving limiter in reducing the artificial dissipation will be compared against other limiters and the effect of the higher central gradient and the scaledown factor. Conclusions and plans for further improvements are given in Sec. IV.

II. Numerical Algorithms

A. Navier–Stokes Solver

The compressible Navier–Stokes (NS) equations are discretized with a hybrid finite volume finite element method [23]. Convective

finite volume fluxes are calculated using a second-order upwind MUSCL variable reconstruction scheme on median dual control volumes. The viscous terms are discretized with linear finite element shape functions on tetrahedral elements. The approximate Riemann solver of Roe is adopted for the calculation of convective fluxes

$$\mathcal{F}_{ij}^{\text{Roe}} = \frac{1}{2}(\mathbf{F}_i + \mathbf{F}_j) - \frac{\alpha}{2}\mathbf{P}_c^{-1}\left|\mathbf{P}_c\frac{\partial \mathbf{F}}{\partial \mathbf{U}}\right|(\mathbf{U}_j - \mathbf{U}_i) \tag{1}$$

where $\mathbf{P}_c$ is the low-speed preconditioning matrix for conservative variables [24–26].

An implicit second-order Euler backward time discretization is employed, where convective and viscous fluxes are linearized and their corresponding Jacobians are evaluated at the previous time step. As the calculation of spatially second-order accurate convective Jacobians is difficult, a first-order approximation is used. To improve the spatial accuracy of the scheme for unsteady simulations, two or three Newton iterations are performed at each time step [27].

The linear system of discretized equations are solved using the generalized minimal residual method (GMRES) [28]. To enhance the convergence of the flow solver, the block Jacobi and the low-speed preconditioners [25,29] are implemented.

B. Turbulence Models

The Spalart–Allmaras (SA) one-equation turbulence model [30] is used to calculate the turbulent viscosity for RANS simulations. The discretization of the SA equation is similar to the NS equations; i.e., convective fluxes are calculated using a second-order finite volume MUSCL scheme while the diffusive and source terms are discretized using linear finite element shape functions on tetrahedral elements.

The implementation of the DDES scheme [9] is based on the substitution of the distance to the wall d in the turbulence equation, with the following length scale:

$$\tilde{d} = d - f_d \text{MAX}(0, d - C_{\text{DES}}\Delta) \tag{2}$$

The function f_d is close to unity in the LES region; it is diminished in the attached boundary layer (RANS region) and in the irrotational zones. The functional form of f_d can be found in [9].

In our baseline RANS scheme, the coefficient α in Eq. (1) is equal to unity, whereby the original Roe flux is retrieved. In the baseline DES scheme, to reduce the artificial dissipation of the convective flux calculation scheme in the LES region and improve the resolution of turbulent eddies, the upwind part of the Roe flux (1) is scaled down by the following factor [19]:

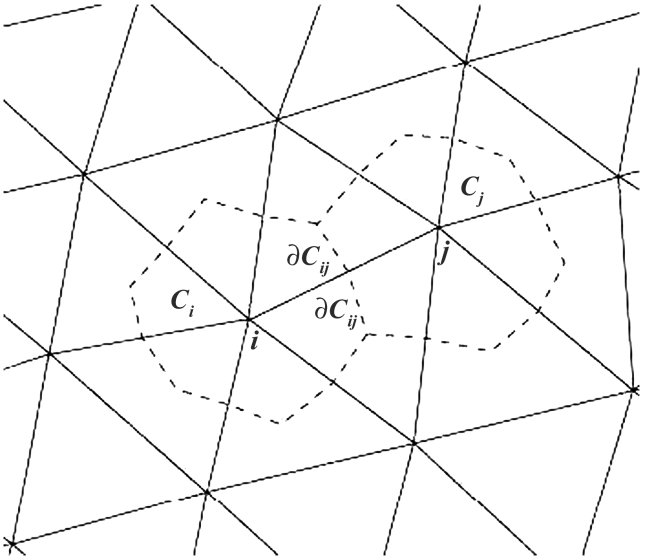

Fig. 1 Median dual control volumes constructed on a 2-D triangular grid, the boundary interface between control volumes C_i and C_j is specified by ∂C_{ij}.

$$\alpha = \max(\alpha_{\min}, 1 - f_d) \tag{3}$$

The scaledown factor α takes a small value $\alpha_{\min}$ in the LES region and is equal to unity in the RANS and irrotational zones. The optimal values of the DES coefficient C_{DES} and the minimum scaledown factor, $\alpha_{\min}$, for the described discretization algorithm, are equal to 0.51 and 0.015, respectively [19]. They are determined through a calibration process [31] involving the simulation of the DIT in a periodic box and the comparison of the calculated energy spectra with the direct numerical simulation (DNS) data [32].

C. Variable Reconstruction and van Albada Limiter

The current implementation of the second-order MUSCL scheme is based on the linear interpolation of primitive variables $\mathbf{V} = [\rho, v_x, v_y, v_z, p]^T$ on boundaries of control volumes in the computational domain, Fig. 1. Primitive variables on ∂C_{ij}, boundary interface of C_i, and C_j control volumes are interpolated using the following combination of central and upwind increments of corresponding variables in the direction of edge $\mathbf{s}_{ij}$ [33]:

$$\mathbf{V}_i^+ = \mathbf{V}_i + \frac{\Phi_i}{4}[(1-\kappa)\mathbf{\Delta}_i^u + (1+\kappa)\mathbf{\Delta}_{ij}^c]$$
$$\mathbf{V}_j^- = \mathbf{V}_j - \frac{\Phi_j}{4}[(1-\kappa)\mathbf{\Delta}_j^u + (1+\kappa)\mathbf{\Delta}_{ij}^c] \tag{4}$$

The upwind and central increments are computed as below:

$$\mathbf{\Delta}_{ij}^c = \mathbf{V}_j - \mathbf{V}_i, \qquad \mathbf{\Delta}_i^u = 2\nabla\mathbf{V}_i \cdot \mathbf{s}_{ij} - (\mathbf{V}_j - \mathbf{V}_i)$$
$$\mathbf{\Delta}_j^u = 2\nabla\mathbf{V}_j \cdot \mathbf{s}_{ij} - (\mathbf{V}_j - \mathbf{V}_i) \tag{5}$$

where $\mathbf{s}_{ij} = \mathbf{x}_j - \mathbf{x}_i$. Nodal gradients $\nabla\mathbf{V}_i$ and $\nabla\mathbf{V}_j$ are calculated as the volumetric average of elemental gradients over all tetrahedral elements connected to nodes i and j, respectively [23]. Finally, flow gradients in each tetrahedral element are obtained using the finite element formulation with linear shape functions.

Functions Φ_i and Φ_j are slope limiters that aim to preserve the total variational diminishing (TVD) property for the second-order spatial discretization. We adopted the van Albada limiter, which is continuously differentiable and is given by

$$\Phi_\cdot = \begin{cases} 0 & \text{if } \mathbf{\Delta}_{ij}^c \mathbf{\Delta}_\cdot^u < 0 \\ \frac{2\mathbf{\Delta}_{ij}^c \mathbf{\Delta}_\cdot^u + \epsilon}{[\mathbf{\Delta}_{ij}^c]^2 + [\mathbf{\Delta}_\cdot^u]^2 + \epsilon} & \text{otherwise} \end{cases} \tag{6}$$

where $\cdot \in i, j$.

The degree of the approximation, in Eq. (4), can be controlled by parameter $-1 \le \kappa \le 1$. In our baseline variable reconstruction scheme, we set $\kappa = \frac{1}{3}$, which is shown by van Leer [33] to result in a third-order accurate scheme on uniform structured grids. Larger values of κ lead to the further reduction of the artificial dissipation; in the limit case of $\kappa = 1$, a purely central and unstable convective flux calculation scheme is obtained.

D. Minimal Vorticity Dissipation Limiter of Löhner

The basic idea of the Löhner's vorticity-preserving limiter [21] is to prevent the slope limiter to be activated (or to use a less dissipative limiter) during the reconstruction of the velocity component along

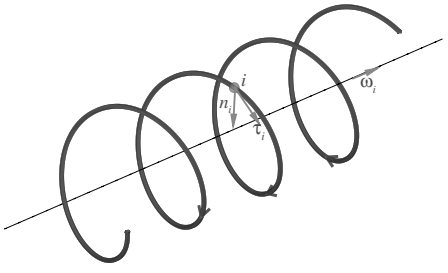

Fig. 2 Orientation of vortex principle axes where the swirl plane is perpendicular to the vortex longitudinal axis.

the tangential direction of a vortex. The velocity component in τ_i-direction at point i, Fig. 2, is always at its extremal (maximum or minimum) value compared with those of its neighboring points in the plane of rotation of a vortex, where τ_i is the direction of the tangential velocity at point i. Slope limiters such as the van Albada limiter, Eq. (6), lower the spatial accuracy of the MUSCL scheme to first order in the presence of a local minimum or maximum. Consequently, the artificial dissipation of the scheme is increased. Löhner's limiter tends to avoid this additional dissipation by inactivating the limiter in the τ-direction.

The two main components of the vorticity-preserving limiter are a sensor to identify the presence of the vortex in the flowfield and transformation matrices between the grid's Cartesian coordinate system, $\mathcal{S}_0(x, y, z)$ and the local vortex system, $\mathcal{S}_\omega(n, \omega, \tau)$, Fig. 2. One of the vortex-identification sensors suggested by Löhner [21] and adopted in the current implementation is the helicity sensor given by

$$\sigma_\omega = \frac{h|\boldsymbol{\omega}|}{\max(\varepsilon, |\mathbf{v}|)} \tag{7}$$

Vortical regions are distinguished where σ_ω is greater than a given threshold value η_ω, and h and ε are defined as

$$h^2 = \frac{\boldsymbol{\omega}\cdot\mathbf{v}}{|\boldsymbol{\omega}||\nabla|\boldsymbol{\omega}||}, \qquad \varepsilon = h^2|\nabla|\boldsymbol{\omega}||| \tag{8}$$

Orthonormal vectors of the local vortex coordinate system $\mathcal{S}_\omega(n, \omega, \tau)$ are calculated using the local vorticity vector $\boldsymbol{\omega}$ and its gradient $\nabla|\boldsymbol{\omega}|$ as defined below [21]:

$$\hat{\boldsymbol{\omega}} = \frac{\nabla\times\mathbf{v}}{|\nabla\times\mathbf{v}|}, \qquad \hat{\mathbf{n}} = \frac{\nabla|\boldsymbol{\omega}|}{|\nabla|\boldsymbol{\omega}||}, \qquad \hat{\boldsymbol{\tau}} = \frac{\hat{\mathbf{n}}\times\hat{\boldsymbol{\omega}}}{|\hat{\mathbf{n}}\times\hat{\boldsymbol{\omega}}|} \tag{9}$$

The calculation of mappings between $\mathcal{S}_0$ and $\mathcal{S}_\omega$ is then straightforward

$$[\mathbf{M}]\colon \mathcal{S}_0 \mapsto \mathcal{S}_\omega \qquad [\mathbf{M}] = \begin{bmatrix} \hat{n}_x & \hat{n}_y & \hat{n}_z \\ \hat{\omega}_x & \hat{\omega}_y & \hat{\omega}_z \\ \hat{\tau}_x & \hat{\tau}_y & \hat{\tau}_z \end{bmatrix} \tag{10}$$

The inverse transformation from $\mathcal{S}_\omega$ to $\mathcal{S}_0$ is given by $[\mathbf{M}]^{-1} = [\mathbf{M}]^T$. The algorithm for implementing the minimal vorticity dissipation limiter is described in [21].

E. Eddy-Preserving Limiter

The concept of the minimal vorticity dissipation limiter is further expanded in this section to develop a slope-limiting algorithm capable of preserving eddies of arbitrary orientations and strengths. The spatial and temporal discretization is required to be fine enough to properly resolve eddies, however, we impose no further requirement on the orientation or the strength of eddies. The configuration of an eddy in Löhner's algorithm described in Sec. II.D is determined via its axial direction spanned by $\hat{\boldsymbol{w}}$ and its plane of rotation spanned by $\hat{\boldsymbol{\tau}}$ and $\hat{\mathbf{n}}$, Fig. 2, which implies that the eddy's axial direction is perpendicular to its plane of rotation. This assumption is by no means general, particularly for stochastic turbulence eddies (coherent structures) that undergo stretching and bending as a result of the flow strain field, Fig. 3. Furthermore, a turbulent flowfield contains a spectrum of eddies with a wide range of strengths, hence the specification of a single threshold value η_ω for the helicity sensor becomes ambiguous. These issues are addressed in the development of the eddy-preserving limiter described below; e.g., vortices are identified based on the existence of complex eigenvalues for the velocity gradient tensor regardless of their vorticity magnitudes or a helicity-based strength sensor. Moreover, principle axes of a vortex are determined using the eigenvectors of the same tensor and no assumption is made concerning their relative orientation.

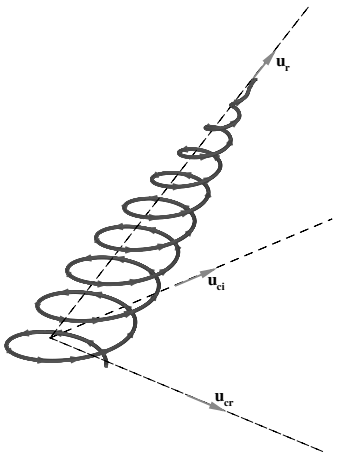

Fig. 3 Principle axes of a typical vortex undergoing deformation due to the flow strain field.

To identify vortical flow regions where the eddy-preserving limiter is activated, one of the popular vortex-identification criteria, particularly λ_2-criterion of Jeong and Hussain [34] or enhanced swirling strength criterion of Chakraborty et al. [22], can be employed. The latter is selected herein since it leads to the same eigenvalue problem that later on will be used to obtain the vortex orientation. This criterion is an enhancement of the vortex definition proposed by Chong et al. [35], whereby in a vortical region, the velocity gradient tensor $\nabla\mathbf{v}$ possesses a conjugate pair of complex eigenvalues; i.e., its spectrum is given by

$$\sigma(\nabla\mathbf{v}) = \{\lambda_r, \lambda_{cr} + \imath\lambda_{ci}, \lambda_{cr} - \imath\lambda_{ci}\}, \quad \text{where } |\lambda_{ci}| > \epsilon \tag{11}$$

Chakraborty et al. [22] added a local measure for the orbital compactness of the vortical motion to Chong's criterion. They further limit the vortical regions to areas where in addition to Eq. (11) the following condition is satisfied:

$$-\beta \le \frac{\lambda_{cr}}{\lambda_{ci}} \le \delta \tag{12}$$

where the values of β and δ determine the orbital compactness of the vortex. In summary, the eddy-preserving limiter is activated where both Eqs. (11) and (12) are valid. These conditions deal with the existence and the quality of the orbital motion of the flow, independent of its strength quantified by vorticity or helicity magnitude.

To calculate the local orientation of a vortex, the relative motion of two nearby points, located at $\mathbf{r}$ and $\mathbf{r} + \delta\mathbf{r}$, is investigated. A second-order accurate spatial expansion of the velocity field around the reference point $\mathbf{r}$ yields to [36]

$$\mathbf{v}(\mathbf{r} + \delta\mathbf{r}) = \mathbf{v}(\mathbf{r}) + \nabla\mathbf{v}\cdot\delta\mathbf{r} + \mathcal{O}(|\delta\mathbf{r}|^2) \tag{13}$$

The relative local trajectory of the nearby point can be calculated via integrating the system of differential Eqs. (13). To decouple the equations, velocity gradient tensor is decomposed into the following form:

$$\nabla\mathbf{v} = [\mathbf{u}_r \quad \mathbf{u}_{cr} \quad \mathbf{u}_{ci}] \begin{bmatrix} \lambda_r & 0 & 0 \\ 0 & \lambda_{cr} & \lambda_{ci} \\ 0 & -\lambda_{ci} & \lambda_{cr} \end{bmatrix} [\mathbf{u}_r \quad \mathbf{u}_{cr} \quad \mathbf{u}_{ci}]^{-1} \tag{14}$$

The transformation matrix from the $\mathcal{S}_0$ system into the system spanned by eigenvectors $\mathbf{u}_r$, $\mathbf{u}_{cr}$, and $\mathbf{u}_{ci}$, is given by

$$[\mathbf{M}] = [\mathbf{u}_r \quad \mathbf{u}_{cr} \quad \mathbf{u}_{ci}]^{-1} \tag{15}$$

Equation (13) in the new system is written as

$$\mathbf{v}'(\mathbf{r}' + \delta\mathbf{r}') \cong \mathbf{v}'(\mathbf{r}') + \begin{bmatrix} \lambda_r & 0 & 0 \\ 0 & \lambda_{cr} & \lambda_{ci} \\ 0 & -\lambda_{ci} & \lambda_{cr} \end{bmatrix} \delta\mathbf{r}' \tag{16}$$

Because of the presence of the complex eigenvalues, the velocity gradient tensor can no longer be completely diagonalized without introducing imaginary numbers. The local trajectory of the fluid

particle in the transformed system at time t is then calculated as below,

$$
\begin{aligned}
r'_r(t) &= r'_r(0)e^{\lambda_r t}\\
r'_{cr}(t) &= e^{\lambda_{cr} t}[r'_{cr}(0)\cos(\lambda_{ci}t) + r'_{ci}(0)\sin(\lambda_{ci}t)]\\
r'_{ci}(t) &= e^{\lambda_{cr} t}[r'_{ci}(0)\cos(\lambda_{ci}t) - r'_{cr}(0)\sin(\lambda_{ci}t)]
\end{aligned}
\tag{17}
$$

where $r'_r(0)$, $r'_{cr}(0)$, and $r'_{ci}(0)$ represent the initial location of the particle in the transformed system. The fluid motion in the $\mathbf{u}_{cr}$ and $\mathbf{u}_{ci}$ direction remains coupled, which indicates the existence of a swirling motion on the plane spanned by these two vectors. Vector $\mathbf{u}_r$ determines the axial direction along which the vortex can be either stretched or contracted.

The normalized eigenvectors of the velocity gradient tensor, hence, construct the unit vectors spanning the local vortex system $\mathcal{S}_\omega(\hat{\mathbf{u}}_r, \hat{\mathbf{u}}_{cr}, \hat{\mathbf{u}}_{ci})$, and the following transformation represents the mapping between the Cartesian grid coordinates and the vortex system:

$$
[\hat{\mathbf{M}}]\colon \mathcal{S}_0 \mapsto \mathcal{S}_\omega \qquad [\hat{\mathbf{M}}] = [\,\hat{\mathbf{u}}_r \quad \hat{\mathbf{u}}_{cr} \quad \hat{\mathbf{u}}_{ci}\,]^{-1} \tag{18}
$$

$\mathcal{S}_\omega$ is, in general, a nonorthogonal system. Using the normalized eigenvectors, Eqs. (14) and (16) are rewritten as below:

$$
\nabla \mathbf{v} = [\,\hat{\mathbf{u}}_r \quad \hat{\mathbf{u}}_{cr} \quad \hat{\mathbf{u}}_{ci}\,]
\begin{bmatrix}
\lambda_r & 0 & 0\\
0 & \lambda_{cr} & \lambda_{ci}\frac{|\mathbf{u}_{cr}|}{|\mathbf{u}_{ci}|}\\
0 & -\lambda_{ci}\frac{|\mathbf{u}_{ci}|}{|\mathbf{u}_{cr}|} & \lambda_{cr}
\end{bmatrix}
[\,\hat{\mathbf{u}}_r \quad \hat{\mathbf{u}}_{cr} \quad \hat{\mathbf{u}}_{ci}\,]^{-1} \tag{19}
$$

$$
\mathbf{v}'(\mathbf{r}' + \delta\mathbf{r}') \cong \mathbf{v}'(\mathbf{r}') +
\begin{bmatrix}
\lambda_r & 0 & 0\\
0 & \lambda_{cr} & \lambda_{ci}\frac{|\mathbf{u}_{cr}|}{|\mathbf{u}_{ci}|}\\
0 & -\lambda_{ci}\frac{|\mathbf{u}_{ci}|}{|\mathbf{u}_{cr}|} & \lambda_{cr}
\end{bmatrix}
\delta\mathbf{r}' \tag{20}
$$

To avoid the excessive dissipation of eddies, the van Albada limiter will be inactivated for the reconstruction of velocity components on the swirl plane of the vortex along $\hat{\mathbf{u}}_{cr}$ and $\hat{\mathbf{u}}_{ci}$ vectors (v'_{cr} and v'_{ci}); i.e., $\Phi = 1$ in Eqs. (4). Furthermore, larger values of κ, i.e., bigger weighting factors for the central increments, are used for the interpolation of velocity gradients along $\hat{\mathbf{u}}_{cr}$ and $\hat{\mathbf{u}}_{ci}$ vectors on the swirl plane of a vortex, Eq. (4). Because of the significant change of velocity gradients along an edge on the swirl plane, the linear interpolation using nodal upwind gradients $\nabla\mathbf{v}_i$ and $\nabla\mathbf{v}_j$ is quite erroneous and leads to extremely different values of interpolated velocity components on opposite sides of the control volume boundaries, i.e., $|v'^{+}_{cr(ci)_i} - v'^{-}_{cr(ci)_j}| \gg 0$. This makes yet another significant contribution to the excessive dissipation of the vortex. It is therefore alleviated via using larger values of κ while interpolating velocity components v'_{cr} and v'_{ci}.

The foregoing arguments for the occurrence of local extremums of v'_{cr} and v'_{ci} along arbitrary edges on the swirl plane of the vortex ($\mathbf{s} = [0, \Delta r'_{cr}, \Delta r'_{ci}]^T$) can be easily extended to a general arbitrary edge $\mathbf{s} = [\Delta r'_r, \Delta r'_{cr}, \Delta r'_{ci}]^T$. The immediate consequence of decomposition Eq. (20) is that, at a given point, following properties are held for velocity gradients in the local $\mathcal{S}_\omega$ system:

$$
\frac{\partial v'_{cr}}{\partial r'_r} = \frac{\partial v'_{ci}}{\partial r'_r} = 0 \tag{21}
$$

The discrete implication of Eq. (21) is important. Using Eq. (20), $\hat{\mathbf{u}}_{cr}$- and $\hat{\mathbf{u}}_{ci}$-components of the velocity increments along edge $\mathbf{s}$ can be written as below:

$$
\Delta v'_{cr} = \nabla v'_{cr}\cdot\mathbf{s} = \lambda_{cr}\Delta r'_{cr} + \lambda_{ci}\frac{|\mathbf{u}_{cr}|}{|\mathbf{u}_{ci}|}\Delta r'_{ci} \tag{22}
$$

$$
\Delta v'_{ci} = \nabla v'_{ci}\cdot\mathbf{s} = -\lambda_{ci}\frac{|\mathbf{u}_{ci}|}{|\mathbf{u}_{cr}|}\Delta r'_{cr} + \lambda_{cr}\Delta r'_{ci} \tag{23}
$$

Therefore, $\Delta v'_{cr}$ and $\Delta v'_{ci}$ are independent of whether edge $\mathbf{s}$ is extended along the axial direction or is located solely on the swirl plane ($\Delta r'_r = 0$).

The algorithm for the eddy-preserving limiting procedure is described below,

1) At each endpoint i and j of edge $\mathbf{s}_{ij}$, calculate eigenvalues of the velocity gradient tensor $\nabla\mathbf{v}$. If the velocity gradient tensor has only real eigenvalues at either of the endpoints, then exit and employ the conventional van Albada limiter Eq. (6) with $\kappa = 1/3$.

2) Verify the compactness of the vortical motion at points i and j using Eq. (12). If the flow lacks vortical compactness at either of the endpoints, then exit and employ the conventional van Albada limiter Eq. (6) with $\kappa = 1/3$.

3) Calculate eigenvectors of the velocity gradient tensor at i and j, whereby obtain unit vectors $\hat{\mathbf{u}}_r$, $\hat{\mathbf{u}}_{cr}$, and $\hat{\mathbf{u}}_{ci}$, as well as transformation matrices $[\hat{\mathbf{M}}]_i$ and $[\hat{\mathbf{M}}]_j$ at each endpoint. If the construction of unit eigenvectors fails at both endpoints, then exit and employ the conventional van Albada limiter Eq. (6) with $\kappa = 1/3$.

4) Define the edge vortex system $\bar{\mathcal{S}}_\omega(\bar{\hat{\mathbf{u}}}_r, \bar{\hat{\mathbf{u}}}_{cr}, \bar{\hat{\mathbf{u}}}_{ci})$ according to the following conditions:

$$
\bar{\mathcal{S}}_\omega = \begin{cases}
\mathcal{S}_\omega(\hat{\mathbf{u}}_{r_i}, \hat{\mathbf{u}}_{cr_i}, \hat{\mathbf{u}}_{ci_i}) & \text{if } \hat{\mathbf{u}}_r \text{, and } \hat{\mathbf{u}}_{cr} \text{ exist only at end-point } i;\\
\mathcal{S}_\omega(\hat{\mathbf{u}}_{r_j}, \hat{\mathbf{u}}_{cr_j}, \hat{\mathbf{u}}_{ci_j}) & \text{if } \hat{\mathbf{u}}_r, \hat{\mathbf{u}}_{cr} \text{ and } \hat{\mathbf{u}}_{ci} \text{ exist only at end-point } j;\\
\mathcal{S}_\omega(\hat{\mathbf{u}}_{r_i}, \hat{\mathbf{u}}_{cr_i}, \hat{\mathbf{u}}_{ci_i}) & \text{if } |[\hat{\mathbf{M}}]_i^{-1}| \le |[\hat{\mathbf{M}}]_j^{-1}|;\\
\mathcal{S}_\omega(\hat{\mathbf{u}}_{r_j}, \hat{\mathbf{u}}_{cr_j}, \hat{\mathbf{u}}_{ci_j}) & \text{if } |[\hat{\mathbf{M}}]_i^{-1}| > |[\hat{\mathbf{M}}]_j^{-1}|
\end{cases}
\tag{24}
$$

Define the edge transformation matrix $[\bar{\mathbf{M}}]_i$ correspondingly.

5) Transform $\mathbf{v}_i$ and $\mathbf{v}_j$, as well as $\mathbf{\Delta}^c_{ij}$, $\mathbf{\Delta}^u_i$, and $\mathbf{\Delta}^u_j$ (only increments corresponding to velocity components) into the $\bar{\mathcal{S}}_\omega$ system.

6) Calculate $v'^{+}_{r_i}$ and $v'^{-}_{r_j}$ using Eq. (4) with $\kappa = 1/3$ and conventional van Albada limiter Eq. (6).

7) Calculate $v'^{+}_{cr_i}$, $v'^{-}_{cr_j}$, $v'^{+}_{ci_i}$, and $v'^{-}_{ci_j}$ using Eq. (4) with a higher value of κ compared with that used in the previous step, while the limiter is inactivated $\Phi_i = \Phi_j = 1$.

8) Transform back all interpolated velocity components, $v'^{+}_{r_i}$, $v'^{-}_{r_j}$, $v'^{+}_{cr_i}$, $v'^{-}_{cr_j}$, $v'^{+}_{ci_i}$, and $v'^{-}_{ci_j}$ into the $\mathcal{S}_0$ system.

In the fourth step of the foregoing algorithm, the edge vortex system is defined as the local vortex system at the endpoint where the second norm of the local inverse transformation matrix is smaller. This is an attempt to minimize the artificial dissipation via minimizing the difference between corresponding left and right (+ and −) interpolated values. The upper bound for the second norm of the velocity difference vector in the edge grid system $\bar{\mathcal{S}}_0$ is calculated as

$$
\left\|\begin{bmatrix} v^-_{x_j} - v^+_{x_i}\\ v^-_{y_j} - v^+_{y_i}\\ v^-_{z_j} - v^+_{z_i}\end{bmatrix}\right\| = \left\|[\bar{\mathbf{M}}]^{-1}\begin{bmatrix} v'^{-}_{r_j} - v'^{+}_{r_i}\\ v'^{-}_{cr_j} - v'^{+}_{cr_i}\\ v'^{-}_{ci_j} - v'^{+}_{ci_i}\end{bmatrix}\right\| \le |[\bar{\mathbf{M}}]^{-1}|\left\|\begin{bmatrix} v'^{-}_{r_j} - v'^{+}_{r_i}\\ v'^{-}_{cr_j} - v'^{+}_{cr_i}\\ v'^{-}_{ci_j} - v'^{+}_{ci_i}\end{bmatrix}\right\| \tag{25}
$$

It is emphasized here that this selection is just an attempt to minimize the amount of the artificial dissipation; since the norm of the velocity difference vector on the right-hand side of Eq. (25) is also dependent on the selection of the transformation matrix. Furthermore, a smaller norm of the velocity difference vector (left-hand side) does not, in all cases, guarantee a smaller overall dissipation.

An alternative approach to obtain the edge vortex system $\bar{\mathcal{S}}_\omega$ is to define $\bar{\hat{\mathbf{u}}}_r$, $\bar{\hat{\mathbf{u}}}_{cr}$, and $\bar{\hat{\mathbf{u}}}_{ci}$ as eigenvectors of the velocity gradient tensor calculated on a coarse level grid containing the reference edge. Since a vortex is by definition a nonlocal flow feature, this approach

complies better with the vortex physics. While the definition of the vortex system based on local fine grid velocity gradients involves some level of nonlocality due to the extended stencil required for the calculation of velocity gradients, a coarse grid solution provides more nonlocal features to the kinematical description of a vortex.

III. Results

Our objective is to evaluate the performance of the minimal vorticity dissipation limiters described in Secs. II.D and II.E for the resolution of well-defined vortices as well as stochastic turbulence eddies. The test cases considered include the DIT in a periodic box, turbulent flows around the stationary and oscillating NACA0015 wing at high AOAs, and the turbulent flow around NACA0021 airfoil at a poststall condition.

A. Description of Schemes

Various numerical schemes have been investigated; each scheme is devised as a distinct combination of a turbulence modeling strategy (RANS or DES) and a slope limiter (van Albada, Löhner, or eddy-preserving). The list of various numerical algorithms with corresponding values for the constants appeared in the numerical formulations of the previous chapters is given by Table 1.

The presence of vortical structures are determined by threshold values ϵ, ζ, δ, and η_ω; the first three parameters pertain to the enhanced swirling strength criteria of Chakraborty et al. [22] in Eqs. (11) and (12), and last one appears in the helicity sensor of Löhner in Eqs. (7). ϵ is the minimum acceptable value of λ_{ci} below which the eigenvalue is considered a real number. It is set equal to 10^{-6} in all test cases. ζ and δ determine the orbital compactness of the vortex and are both set to $1/\sqrt{3}$. This is based on an argument by Chakraborty et al. [22] to identify the relationship between different vortex-identification criteria. η_ω specifies the minimum helicity of a vortical structure that activates the Löhner limiter. As a variety of vortices of different strengths are investigated in each test case, this threshold is set equal to a rather small value of 0.1.

Parameter $\alpha_{\min}$ is the artificial dissipation scaledown factor in the LES region, as appeared in Eq. (3). Its optimum value is determined in the calibration procedure explained in Sec. III.B. In the original Roe flux formulation no scaledown factor is used; i.e., $\alpha = \alpha_{\min} = 1$; however, in DES schemes, smaller values are required to enhance the resolution of vortices in the LES region. Smaller values of $\alpha_{\min}$ slow down the convergence of the flow solver and can impair the robustness of the scheme. Hence, schemes that can maintain a reasonable accuracy for the captured vortices with higher values of $\alpha_{\min}$ are preferable. The development of DES-E, DES-L, DES-C schemes and their RANS counterparts, where $\alpha_{\min} = 1$, is based on this consideration.

Parameter κ determines the weight of the central and upwind gradients used for the variable reconstruction. The value of $\kappa = 1/3$, as shown by van Leer [33] and Dervieux and Desideri [37], in Eq. (4), results in the third-order spatial accuracy on uniform structured grids. Larger values of κ lead to lower artificial dissipation; e.g., in the extreme case of $\kappa = 1$, the scheme would be purely central and unstable. Ideally, we would like to have the κ value as large as possible provided that no compromise is made with respect to the stability of the scheme. In DES-E, DES-L, DES-C schemes and their RANS counterparts, where the Löhner or the eddy-preserving limiter is activated, a larger value of $\kappa = 0.8$ is employed for the interpolation of specific components of the velocity as described in Secs. II.D and II.E. Where no vortex is detected, all variables are interpolated using $\kappa = 1/3$.

Table 1 Numerical schemes and constant values

Scheme	Turbulence	Limiter	$\alpha_{\min}$	κ
DES-0	DDES	van Albada	0.015	One-third
DES-C	DDES	van Albada	1	0.8 in vortical region One-third elsewhere
DES-E	DDES	Eddy-preserving	1	0.8 in vortical region One-third elsewhere
DES-E0	DDES	Eddy-preserving	0.3	0.8 in vortical region One-third elsewhere
DES-L	DDES	Löhner	1	0.8 in vortical region One-third elsewhere
DES-VA	DDES	van Albada	1	One-third
RANS-0	RANS	van Albada	1	One-third
RANS-C	RANS	van Albada	1	0.8 in vortical region One-third elsewhere
RANS-E	RANS	Eddy-preserving	1	0.8 in vortical region One-third elsewhere

The optimum value of $\kappa = 0.8$ is determined via some numerical experiments. The experiments include the simulation of a tip vortex in inviscid and viscous flows and the comparison of calculated vortex characteristics at different values of κ. The maximum vorticity and helicity at the center of the vortex are significantly reduced for $\kappa > 0.9$.

DES-0 and RANS-0 schemes are our baseline DES and RANS algorithms. DES-C and RANS-C schemes are similar to DES-E and RANS-E schemes except for the regions where a vortex is detected. The higher value of $\kappa = 0.8$ (instead of $1/3$) is used for reconstruction of all three Cartesian components of velocity in these regions while the transformation step is dismissed. These schemes are devised to investigate the importance of performing the variable reconstruction along the vortex principle axes as it is done in DES-E and RANS-E. The value of $\alpha = 0.3$ *in the DES-E0 scheme is chosen just for the demonstration of how the prediction accuracy for vortex characteristics can be improved by further reducing* α while the eddy-preserving limiter is employed. The same improvements are expected for other schemes; e.g., DES-C and DES-L. The combination of the scaledown parameter, slope limiter, and the parameter κ results to the various schemes presented in Table 1 and are essential in this study to demonstrate the effectiveness of each approach in reducing the artificial dissipation while ensuring a stable scheme.

B. Decay of Isotropic Turbulence

The decay of homogeneous isotropic turbulence in a periodic cube with an equal edge length of 2π is simulated. The turbulence kinetic energy spectra is then compared with available DNS results [32]. The initial velocity field is calculated via filtering the DNS velocity field at the nondimensional time of $t^* = 1.01356$. The reference length and velocity used for the nondimensionalization are equal to unity. The flow is assumed at atmospheric condition, hence the Mach and Reynolds numbers based on the above reference values are equal to 0.003 and 4.82×10^6. The Courant–Friedrichs–Lewy (CFL) number for unsteady flow calculations is fixed and equal to seven. The unstructured tetrahedral mesh is generated by first dividing each edge into 64 equal intervals whereby a structured cubic mesh is created; then each cube is broken into six tetrahedral elements without introducing any additional mesh node.

This is the standard test case used to calibrate the baseline DES scheme (DES-0) and to obtain the optimum C_{DES} and $\alpha_{\min}$ coefficients [19,31]. Furthermore, this test case provides an estimate of the size of the smallest eddies that can be accurately resolved via a given scheme. The scheme is expected to recover the proper energy spectra (turbulent kinetic energy versus eddy wave number k) for the range of eddies from the largest to the smallest resolved eddies of the size of two grid points corresponding to the Nyquist cutoff frequency.

Turbulence kinetic energy spectra calculated using DES-0, DES-VA, DES-L, and DES-E schemes at a nondimensional time of $t^* = 2.018$ are compared with the DNS data in Fig. 4a. The extremely reduced artificial dissipation of DES-0 scheme leads to the best agreement with the DNS spectra at the upper end of the resolved wave numbers close to the Nyquist cutoff frequency of 32. DES-L and DES-E rely on capturing vortices to activate the artificial dissipation reduction scheme. As the smallest properly captured eddies (with resolved distinct core regions) are of the size of approximately 10 edge lengths [20], one expects to obtain proper energy levels at wave numbers smaller than 6–7 given the current

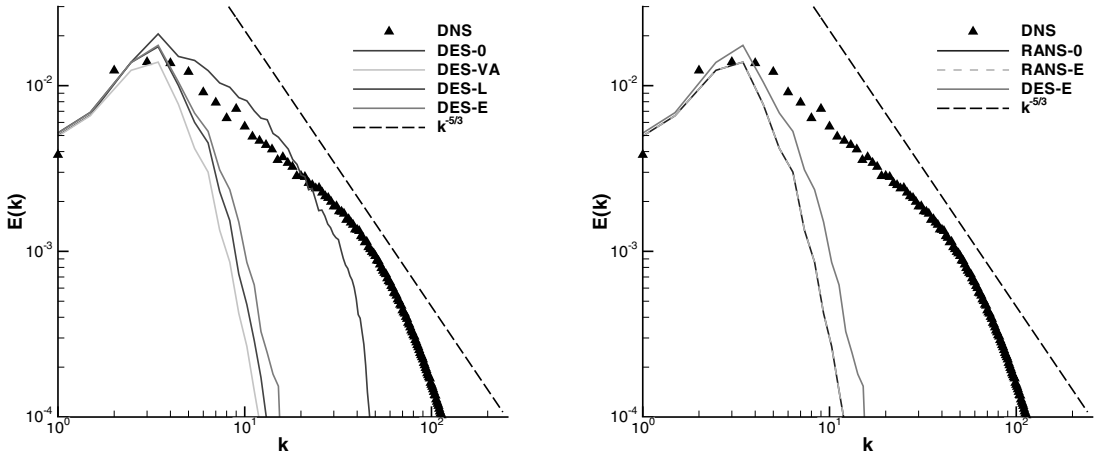

a) DES schemes b) RANS schemes

Fig. 4 Comparison of 3-D turbulence kinetic energy spectra at $t^* = 2.018$ for the decay of isotropic turbulence in a periodic cube with equal edge length of 2π. DES-0, DES-E, DES-L, DES-VA, RANS-0, and RANS-E simulations at a spatial resolution of 64 are compared with DNS data at a spatial resolution of 512.

computational grid. This loss of accuracy is depicted in Fig. 4a as the sudden change of the slope in the turbulence energy spectra curves. DES-VA scheme predicts the lowest amount of kinetic energy spectra in the entire range of resolved wave numbers in comparison to other DES schemes.

A similar comparison has been made in Fig. 4b for RANS-0 and RANS-E schemes. The DES-E spectra is also included for the reference. RANS schemes also exhibit an excessive damping of small eddies. RANS predictions are similar to DES-VA results. The performance of RANS schemes, in particular, has been insensitive to the selection of the artificial dissipation scheme. In fact, RANS-0, RANS-E, and DES-VA schemes result in almost the same energy spectra.

Neither Löhner's limiter nor the eddy-preserving limiter has been capable of predicting an accurate turbulence kinetic energy level for small eddies up to the Nyquist cutoff frequency. To activate the eddy-preserving limiter to reduce the dissipation of eddies, a sufficiently fine spatial and temporal resolutions should be provided to capture the structure of corresponding eddies. The 64^3 resolution on the DIT cube is fine enough for the resolution of eddies with wave lengths smaller that 6–7. This is almost one fifth of the corresponding Nyquist cutoff frequency, which is the upper bound for wave numbers where the energy spectra should be properly resolved in DIT problems.

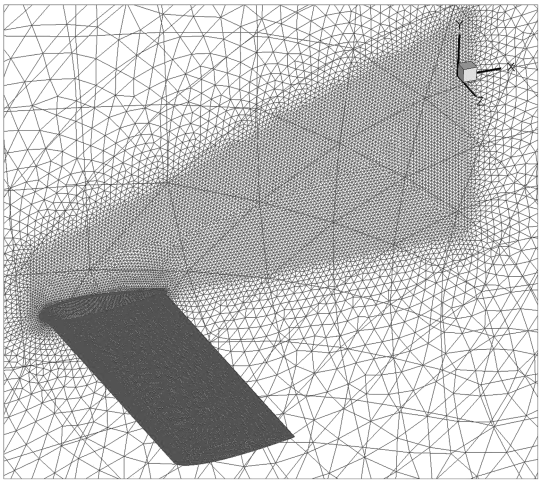

Fig. 5 Unstructured tetrahedral mesh around NACA0015 rectangular wing. The grid contains 2,247,174 nodes and 13,300,570 elements. The dense area above the wing represents the focus region where turbulent eddies are to be captured.

C. NACA0015 Wing at High Angles of Attack

Turbulent flows around a rectangular NACA0015 wing at high AOAs of 12.0°, 14.0°, 16.0° and 18.0° are simulated. Our main objective is to quantitatively evaluate the performance of different schemes in the resolution of a tip vortex. Moreover, qualitative comparisons are made through investigating the quality of resolved turbulence eddies formed on the upper surface of the wing under static stall conditions. The tip vortex characteristics are calculated at a plane normal to the freestream at $x/c = 1$ downstream of the wing trailing edge where the streamwise direction is represented by x, and c indicates the wing chord. Flow solutions are averaged over a period of 1000 time steps for the calculation of tip vortex characteristics. Numerical predictions are compared against the experimental measurements performed by Birch and Lee [38,39].

The computational grid shown in Fig. 5 consists of 2,247,174 grid points and 13,300,570 tetrahedral elements. The mesh is generated to address DES grid requirements described by Spalart [20]; e.g., the focus region above the upper surface of the wing depicted in Fig. 5 contains almost isotropic elements with equal edge length of $0.028c$. The first layer grid spacing from the wall in the RANS region satisfies $y^+ \leq 1$ in the law-of-wall units. The physical time step is equal to $0.008c/V_\infty$, which approximately corresponds to a CFL number of 5000. The wing geometry and freestream conditions are described in Table 2. The flow is at atmospheric condition and the reference length and velocity are equal to the wing chord and the freestream velocity, respectively. Although RANS requirements for the mesh and the time step are generally less stringent than DES, the same mesh and time step are used for RANS simulations to make a fair assessment of the accuracy of each scheme for unsteady flow simulations.

A finer grid with 4,379,053 nodes and 26,064,193 tetrahedra, is also generated through grid refinement by a factor of $\sqrt{2}$ in the focus region. DES results on the coarse and fine grids for the wing at 18° AOA show no significant differences in terms of the averaged resolved features. Simulation results presented in subsequent sections are obtained on the coarse grid.

1. *DES Results*

Tip vortex characteristics calculated using DES-0, DES-E, DES-L, DES-VA, and DES-C are compared with experimental measurements at various AOAs in Figs. 6a–6c. More details about

Table 2 Wing geometry and freestream condition for NACA0015 test case

Chord	Half-span	V_∞	Reynolds number	Mach number
0.203 m	0.508 m	14.4 m/s	1.86×10^5	0.04

the postprocessing of simulation data for the calculation of tip vortex characteristics can be found in a previous work by the same authors [19]. The maximum 2-D vorticity on $x/c = 1$ plane is depicted in Fig. 6a, where the schemes can be ordered, descendingly, with respect to the level of agreement with the experiment as DES-0, DES-E, DES-C, DES-L, and DES-VA. All schemes underpredict the maximum 2-D vorticity. The comparison of DES-0 and DES-VA results demonstrates the effectiveness of the scaledown approach. The sole difference between the two schemes is the extreme artificial dissipation scaledown factor of 0.015 in DES-0, which leads to the sharpest resolution of the tip vortex and the maximum captured 2-D vorticity and tangential velocity and the smallest core radius among all DES schemes. To emphasize the importance of the eddy-preserving limiter, DES-E and DES-C results are compared. The proper selection of the velocity components on the swirl plane of the vortex and the consequent implementation of the eddy-preserving limiter with the use of the larger $\kappa = 0.8$ value for the interpolation result in the second most accurate predictions for the 2-D vorticity on the $x/c = 1$ plane. Further reduction of the artificial dissipation through the use of the larger $\kappa = 0.8$ value for the interpolation of all three Cartesian components of the velocity, in the DES-C scheme, fails to provide a sharper resolution of the 2-D vorticity. Furthermore, DES-C predicts a larger core radius than that is obtained by DES-E, Fig. 6c. We attribute this mainly to the importance of performing the velocity component reconstruction along the vortex principle axes. The artificial dissipation reduction for a single component of the velocity in the DES-L algorithm is insufficient to provide a significant improvement over DES-VA results for the resolution of the planar vorticity. No artificial dissipation reduction treatment is employed in the latter algorithm, which results in the most prominent dissipation of the vortex and the lowest captured 2-D vorticity levels.

A similar trend can be observed in Fig. 6b for the maximum captured tangential velocity on the $x/c = 1$ plane where all schemes underpredict the tangential velocity and they can be ordered in terms of the accuracy of the predictions as DES-0, DES-E, DES-C, DES-L, and DES-VA. Likewise, Fig. 6c follows the same trend. However, as explained in the preceding paragraph, the difference between the DES-E and DES-C schemes is more pronounced in this figure.

The convergence of different DES schemes are compared in Fig. 7a. The plot shows the residual reduction of the GMRES algorithm in a typical time step. Because of a significantly lower artificial dissipation, $\alpha = 0.015$, DES-0 requires, at least, 2.5 times more iterations compared with other DES schemes to achieve a residual reduction of 6 orders of magnitude. DES-E, DES-L, and DES-VA show more or less the same convergence behavior, with DES-VA being slightly faster. Since the cost of local eigenvalue calculations is negligible compared with the cost of matrix-vector product operations in GMRES algorithm, the 2.5 fold reduction in

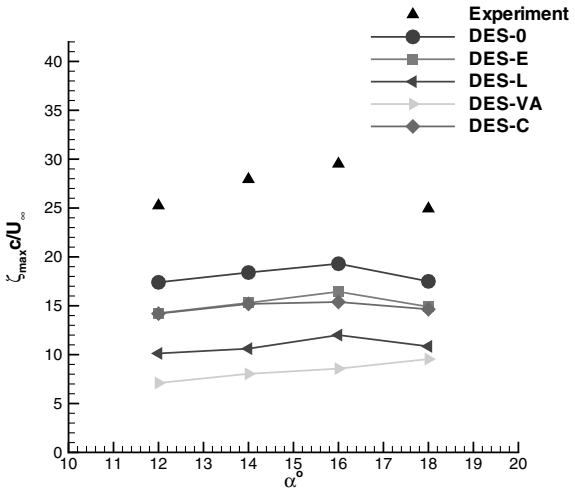

a) Maximum 2D vorticity

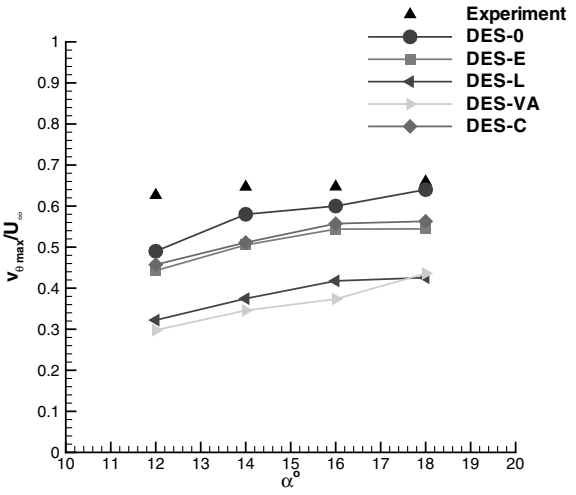

b) Maximum tangential velocity

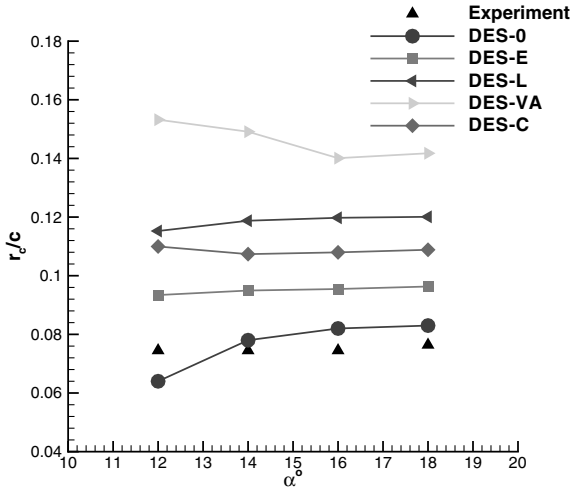

c) Core radius

Fig. 6 Vortex statistics at different AOAs. Maximum planar vorticity, maximum tangential and core radius of the tip vortex are calculated at $x/c = 1$ plane downstream of the trailing. DES-0, DES-E, DES-L, DES-VA, and DES-C predictions are compared with the experimental data.

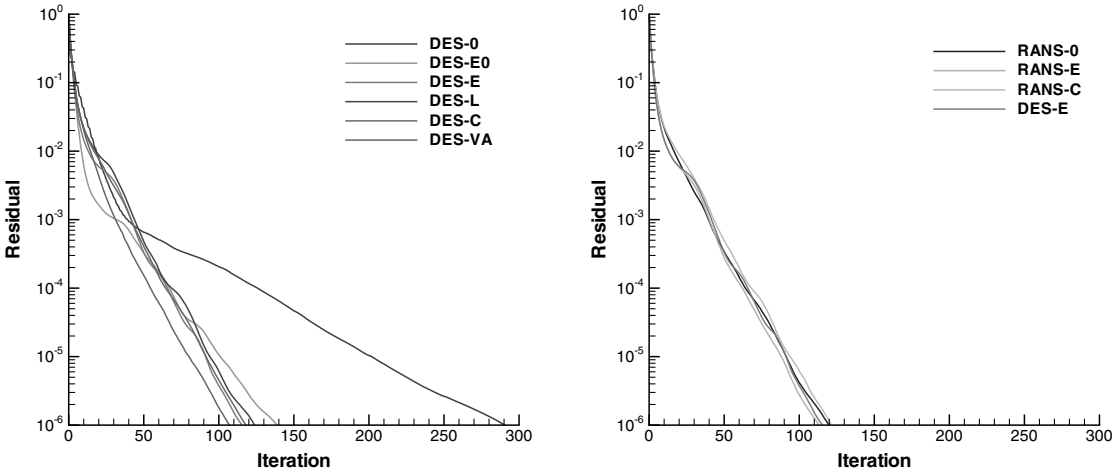

a) DES schemes b) RANS schemes

Fig. 7 Residual reduction versus GMRES iterations in a typical time step for the flow around NACA0015 wing at 18° AOA. Part a) DES-E0, DES-E, DES-L, DES-C, and DES-VA schemes are compared with the baseline scheme, DES-0; and part b) RANS-E, RANS-C, and DES-E schemes are compared with the baseline RANS scheme, RANS-0.

the number of iterations leads to a 2.5 fold speedup in terms of the computational time.

The artificial dissipation reduction scheme is activated in a significantly smaller region within the computational domain for DES-E runs in comparison to the DES-0 results, Figs. 8a and 8b. Regions where the scaledown factor is at its minimum value of 0.015 in the case of DES-0, or areas where the eddy-preserving limiter is active in the case of DES-E are indicated with the red color in this figure. For the DES-0 scheme, except in a small region in the vicinity of the wing surface, the artificial dissipation scaledown is fully active in the entire computational domain. The implementation of another scaledown function proposed by Travin et al. [16] led to no significant reduction in the extent of this area. The eddy-preserving limiter, however, is only activated where vortical structures are detected. This considerably limits the red zone and contributes to the faster convergence of the scheme.

The accuracy of DES-E can be further improved by scaling down the artificial dissipation of the flux calculation scheme; e.g., in the DES-E0 scheme the artificial dissipation (upwind) part of convective fluxes for all five conservative variables are scaled down by a factor of 0.3 in the LES region of the flow, i.e., $\alpha_{\min} = 0.3$. Figure 9 shows vortex characteristics calculated using DES-0, DES-E0, and DES-E schemes. The accuracy of numerical predictions for maximum tangential velocity and the core radius is almost identical for DES-E0 and DES-0 schemes. This enhanced accuracy is achieved at the expense of a slower convergence; DES-E0 exhibits only a two fold faster convergence rate than that of the baseline DES-0, Fig. 7a. The agreement between the experimental data and the simulation is slightly improved if the scaledown factor is further decreased to $\alpha_{\min} = 0.2$. Both values of $\alpha_{\min} = 0.2$ *and* 0.3 provide a good agreement with the experimental data for the maximum tangential velocity and the core radius calculated from simulations. To achieve a good agreement for the maximum planar vorticity is more challenging, e.g., the calculated values are extremely sensitive to the grid spacing on $x/c = 1$ plane.

Turbulence eddies resolved using various DES schemes are compared in Figs. 10a–10f. These figures correspond to the wing at the static stall condition at an AOA of 18°. DES-E0 provides the closest resolution to that obtained using the baseline DES scheme. DES-VA scheme is unable to capture the shedding of vortices. Although it predicts flow separations covering the entire upper surface of the wing, the reversed flow regions remain in close proximity of the surface and no shedding is predicted. Whereas, in all other schemes involving an artificial dissipation reduction algorithm, unsteady vortex shedding phenomena is observed. This highlights the importance of the artificial dissipation reduction algorithms to more accurately capture the flow physics on the upper surface of the wing.

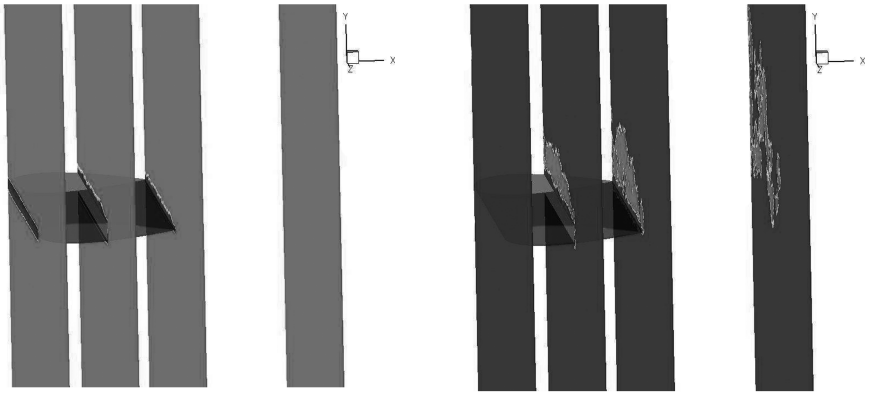

a) DES-0 scheme b) DES-E scheme

Fig. 8 Contour plots indicating regions where the artificial dissipation reduction scheme is active. Contours are depicted on several planes normal to the wing's chordwise direction. The light grey regions represent areas where either the scaledown factor is at its minimum value or the eddy-preserving limiter is activated.

2. RANS Results

RANS-0, RANS-E, and RANS-C predictions are compared in Figs. 11a–11c with experimental measurements. DES-E results are also included in these figures for reference. RANS-E and RANS-C significantly outperform the baseline RANS schemes. In fact, DES-E, RANS-E, and RANS-C predictions are quite close; DES-E shows a slightly better accuracy. The enhanced performance of the RANS-E scheme compared with other RANS schemes is obtained with a minimal cost in terms of the convergence rate or the computational time; as depicted in Fig. 7b, the convergence rates of RANS-0, RANS-E, and RANS-C are almost identical.

The convergence of different RANS schemes are compared with the DES-E scheme in Fig. 7b. The plot indicates almost the same convergence rate for DES-E and all RANS schemes regardless of the type of the implemented artificial dissipation reduction algorithm.

Turbulence eddies resolved using various RANS-0 and RANS-E schemes are compared in Figs. 12a and 12b. The wing is at a poststall condition at an AOA of 18°. RANS-E clearly performs a superior job, compared with the baseline method, to capture the shedding of vortices from the upper surface of the wing. RANS-0 predicts the flow separation from the entire upper surface of the wing [19], however, the reversed flow region similar to what is observed in DES-VA results, is bounded to a small distance from the wing upper surface without triggering the vortex shedding phenomena.

D. NACA0021 Airfoil at High Angle of Attack

The turbulent separated flow around NACA0021 airfoil at 60° AOA is simulated. This is one of the standard test cases used for the validation of DES implementations in the DESider project [40]. The available experimental data that are obtained via postprocessing of pressure measurements include the average lift and drag coefficients, average pressure distribution around the airfoil, and the frequency content of the lift coefficient [40,41]. This provides a suitable database to assess the performance of different numerical schemes studied in this paper. In the postprocessing of the numerical simulation data, average values and frequency contents are calculated in an interval of 4000–5000 time steps excluding the first transient 200 time steps. A smaller interval of 2500 time steps, however, yielded to no significant changes in the major features captured in the postprocessed data.

The computational grid is shown in Fig. 13. It contains 3,726,534 mesh points and 22,076,935 tetrahedral elements. DES grid generation guidelines are followed herein; e.g., $y^+ \leq 1$ criterion is satisfied in the RANS region and the focus region contains nearly uniform isotropic distribution of tetrahedral elements with an almost equal edge length of $0.025c$. The edge lengths gradually increase at a very small growth rate of 1.02 farther from the airfoil surface in the focus region. The physical time step is equal to $0.0125c/V_\infty$, which approximately corresponds to a CFL number of 8000. The airfoil

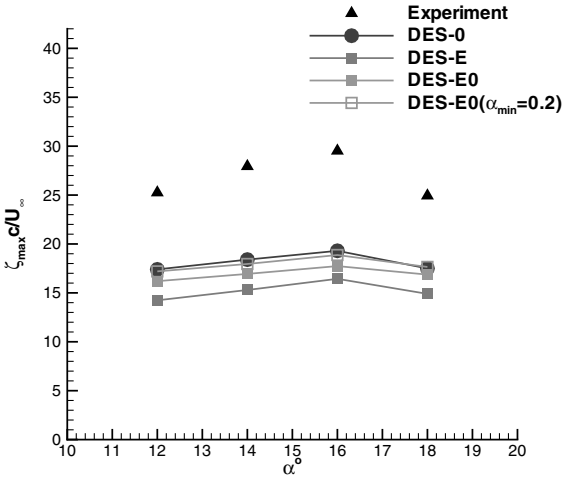

a) Maximum 2D vorticity

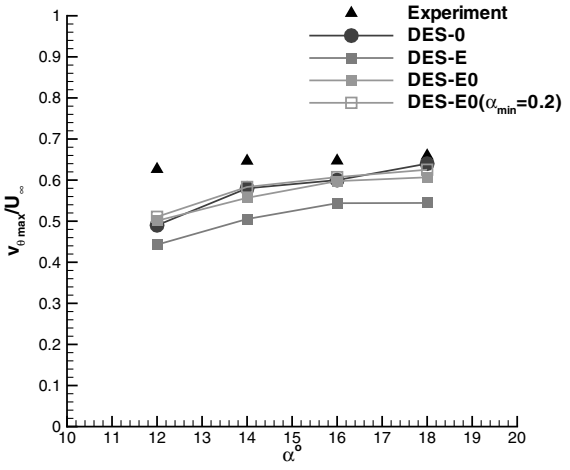

b) Maximum tangential velocity

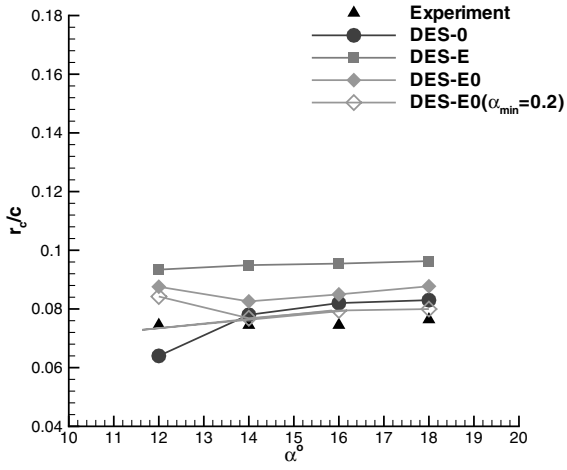

c) Core radius

Fig. 9 Vortex statistics at different AOAs. Maximum planar vorticity, maximum tangential and core radius of the tip vortex are calculated at $x/c = 1$ plane downstream of the trailing. DES-0, DES-E, and DES-E0 predictions are compared with the experimental data.

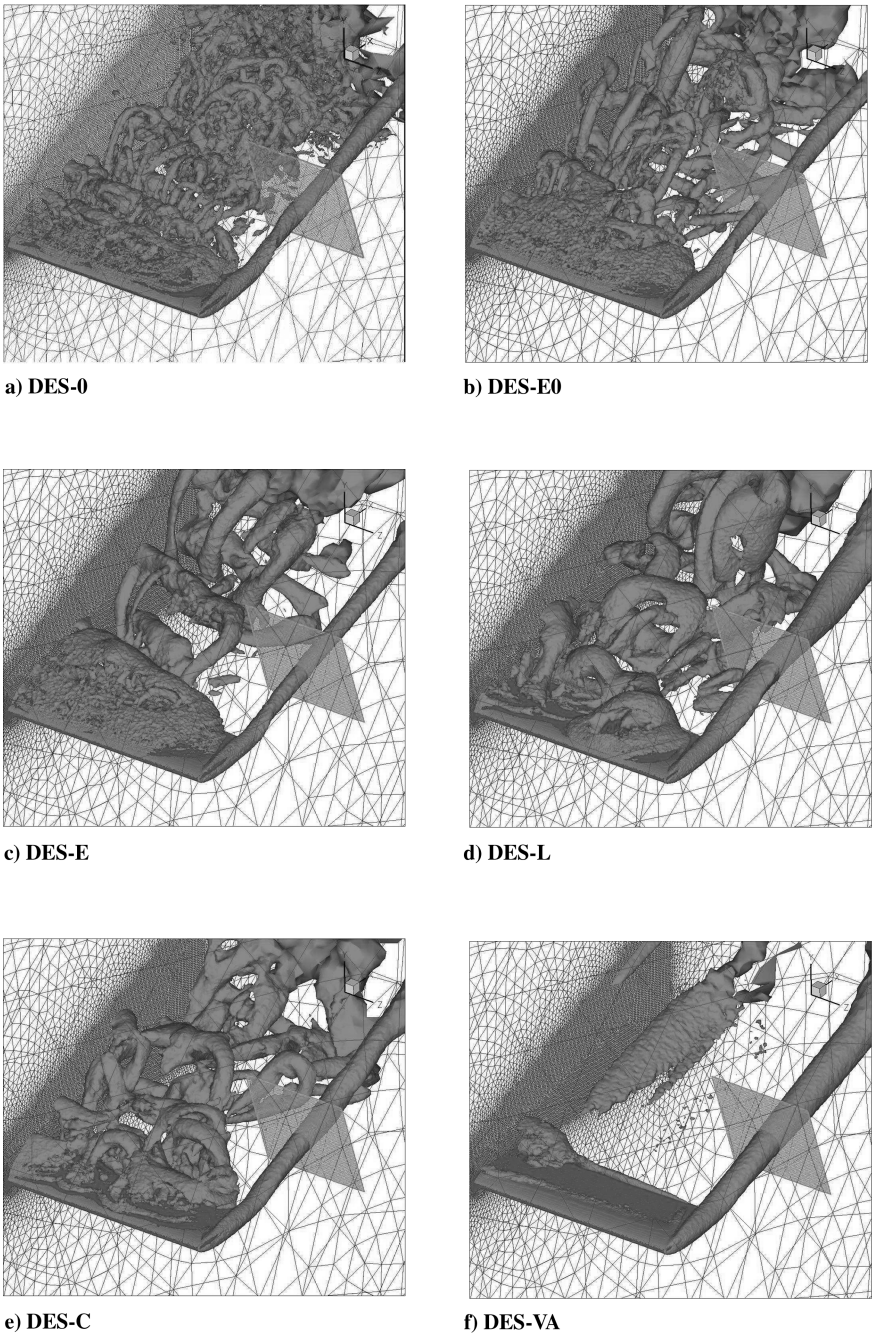

a) DES-0 **b) DES-E0**

c) DES-E **d) DES-L**

e) DES-C **f) DES-VA**

Fig. 10 λ_2 isosurfaces for flow around NACA0015 at 18° AOA under static stalls condition. Flowfields calculated using different DES schemes are compared: part a) DES-0; part b) DES-E0; part c) DES-E; part d) DES-L; part e) DES-C; and part f) DES-VA.

geometry and the freestream flow conditions are described in Table 3. The flow is at atmospheric condition.

DES-0 scheme with $\alpha = 0.015$ is unstable in this test case. The scheme remains unstable for $\alpha < 0.3$, hence DES-0 results reported in this section correspond to an augmented coefficient of $\alpha = 0.3$.

Our numerical simulations are also compared with some of the benchmark data of the DESider project [42]. In particular, where data were available [40], the average force coefficient, pressure distribution, and the spectral content of the lift coefficient provided by DLR, German Aerospace Center and National Aerospace Laboratory/NLR (The Netherlands) are included in the comparisons. DLR simulations are performed using an unstructured finite volume compressible NS solver with a second-order accurate discretization in space and time (TAU code). While NLR computations correspond to a block-structured finite volume NS solver where convective fluxes are discretized using a fourth-order accurate scheme [40]. SA-DES and X-LES [42] turbulence modeling are employed in DLR and NLR solvers, respectively. Three different meshes, coarse, medium, and fine, were considered in that study; they consisted of 476,784, 1,588,776, and 5,316,444 mesh points, respectively. The computational domain had a span width of one chord length, however, as mentioned before, a span width of four chord is employed in this work. Our computational grid includes an average of 931,633 grid points in unit span length. As the fine grid simulations were not sufficiently converged, only the coarse and the medium grid data for the spectral content of the lift coefficient and the average pressure distribution around the airfoil are compared with our simulation results.

1. DES Results

Pressure coefficient distribution around the airfoil calculated using DES-0, DES-E, DES-L, DES-C, and DES-VA schemes are compared with the experimental measurements in Fig. 14. As the flow remains attached and vortical structures are absent on the lower surface of the wing, all schemes predict the pressure

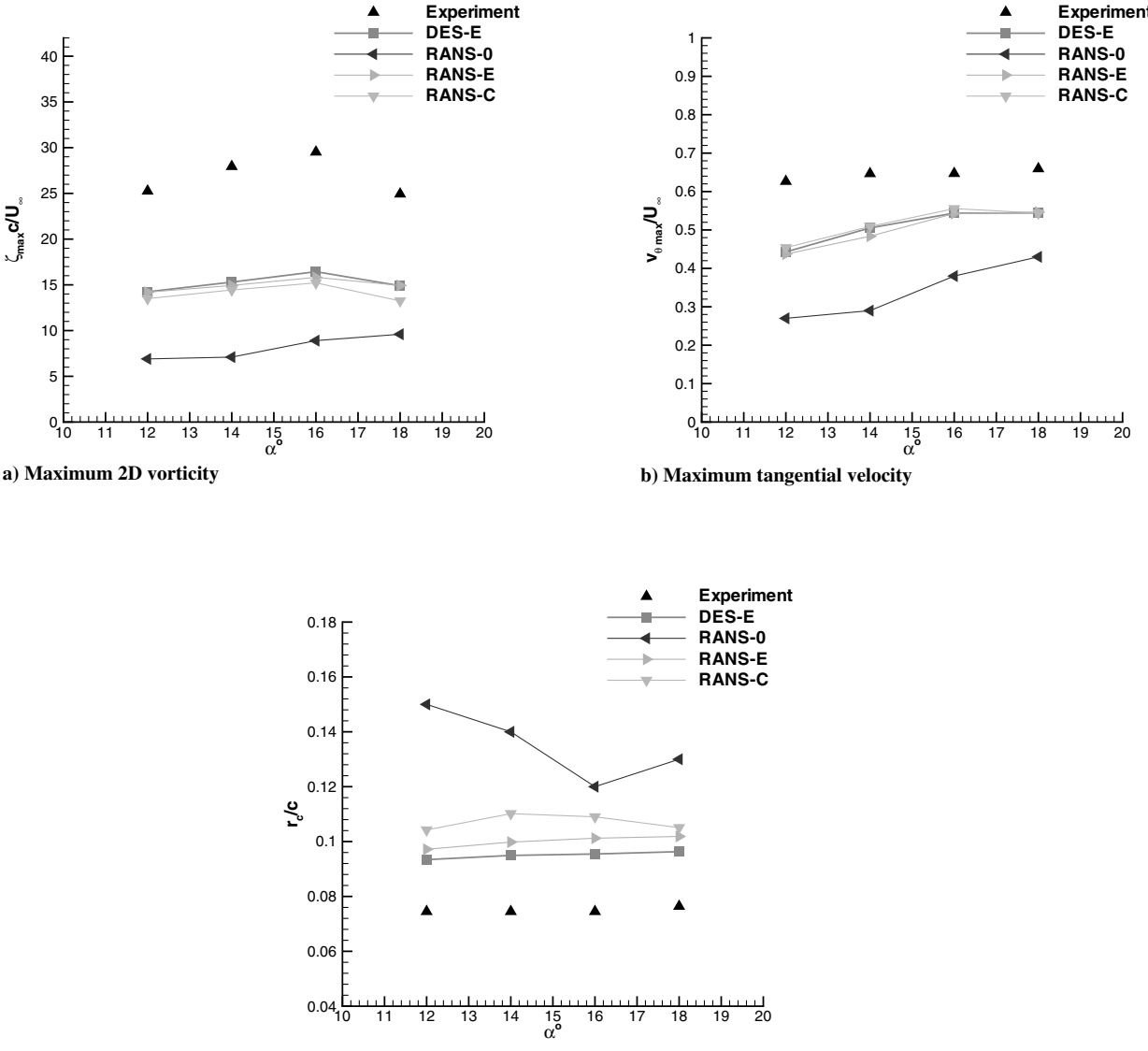

a) Maximum 2D vorticity

b) Maximum tangential velocity

c) Core radius

Fig. 11 Vortex statistics at different AOAs. Maximum planar vorticity, maximum tangential and core radius of the tip vortex are calculated at $x/c = 1$ plane downstream of the trailing. RANS-0, RANS-E, RANS-C, and DES-E predictions are compared with the experimental data.

distribution on the lower surface of the airfoil with more or less the same accuracy. On the upper surface of the wing, DES-L and DES-VA overpredict the pressure, whereas DES-C exhibits a slight underprediction. DES-0 and DES-E simulation results are close, with DES-0 being slightly more accurate.

The average pressure coefficients reported by DLR on the coarse grid and by NLR on the coarse and medium grids are depicted in Fig. 15. The pressure coefficients on the coarse grid are closer to the experimental measurements.

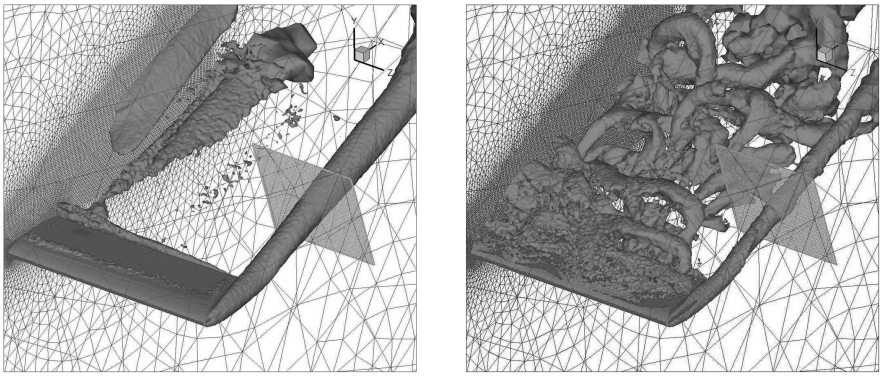

a) RANS-0

b) RANS-E

Fig. 12 λ_2 isosurfaces for flow around NACA0015 at 18° AOA under static stalls condition. Flowfields calculated using different RANS schemes are compared: part a) RANS-0; and part b) RANS-E.

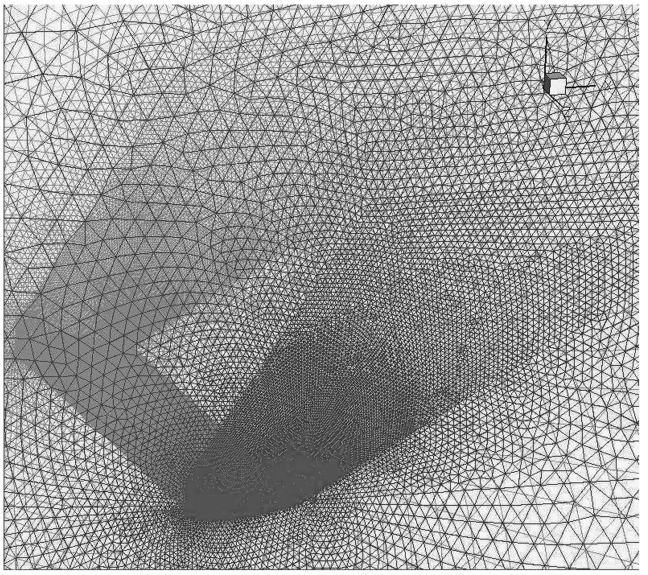

Fig. 13 Unstructured tetrahedral mesh around extruded NACA0021 airfoil. The grid contains 3,726,534 nodes and 22,076,935 elements. The dense area above the wing represents the focus region where turbulent eddies are to be captured.

Table 3 Airfoil geometry and freestream condition for NACA0021 test case

Chord	Span	V_∞	Reynolds number	Mach number
0.125 m	0.500 m	56.3 m/s	2.70×10^5	0.15

Average lift and drag coefficients C_L and C_D are listed in Table 4. It should be clarified that the experimental measurements for lift and drag coefficients are based on the pressure integration of the measured values around the wing surface [41]. The simulation results, however, includes viscous forces. As no tolerance has been reported for the accuracy of the measured force coefficients, the simulation data herein are compared with the exact reported measured values. The closest lift value to the experimental measurement obtained using the DES-E method, while the DES-C scheme results in the least deviation from the measurement for the drag coefficient. All schemes underpredict the drag coefficient. Because of the lack of error bounds for measured values as well as the discrepancy between the type of forces considered in the measurement and those in the numerical simulations, as explained earlier in this paragraph, we feel that the comparison of the performance of different numerical schemes, solely based on the accuracy of the lift and drag values, is inconclusive. The accuracy of DLR and NLR results degrades as the grid becomes finer. The DLR study demonstrated challenges in obtaining a grid converged solution [42].

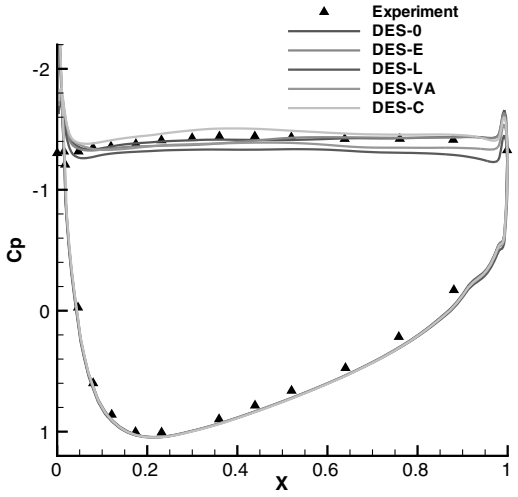

Fig. 14 Average pressure coefficient distribution around NACA0021 airfoil at $Re = 270,000$ calculated using DES-0, DES-E, DES-L, DES-C, and DES-VA schemes.

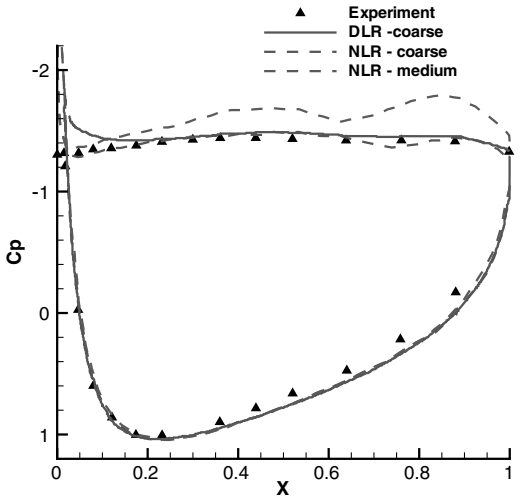

Fig. 15 DESider benchmark data for pressure distribution around NACA0021 airfoil calculated on the coarse grid (DLR) and the coarse and medium grids (NLR) [40].

Spectral contents of the lift coefficient history for DES schemes are depicted in Figs. 16a–16e. Two peaks are present in the experimental measurement at $St = fc/V_\infty \approx 0.2$ and 0.4, where f is the frequency of oscillations in Hz. The challenge is to accurately capture the second peak. Although all DES schemes are capable to resolve the first peak, only the DES-E scheme provides a clear resolution of the second peak. DES-0 shows some noticeable spurious oscillations in the vicinity of the second peak. A small spurious peak is also present before the first peak, at $St \approx 0.12$. These spurious oscillations are significantly amplified in DES-C predictions. DES-L and DES-VA failed to provide a recognizable resolution of the second peak.

DLR prediction for the lift coefficient spectral contents on the coarse and medium grids are depicted in Fig. 16f. Both peaks are captured, however, the resolution of the reported data is insufficient to determine the exact location of the second peak.

The convergence of the flow residual in the GMRES solver at a typical time step are shown in Fig. 17a for DES schemes. Convergence rates of DES-E, DES-L, DES-C, and all RANS schemes are

Table 4 Average lift and drag coefficients for NACA0021 at 60° AOA

Scheme	C_L	ΔC_L	C_D	ΔC_D
DES-0	0.95	0.02	1.49	−0.06
DES-E	0.94	0.01	1.49	−0.06
DES-L	0.88	−0.05	1.37	−0.18
DES-C	0.96	0.03	1.53	−0.02
DES-VA	0.91	−0.02	1.42	−0.13
DLR coarse	0.90	−0.03	1.50	−0.05
DLR medium	0.89	−0.04	1.47	−0.08
DLR fine	1.20	0.27	1.86	0.31
NLR coarse	1.08	0.15	1.53	−0.02
NLR medium	1.17	0.24	1.74	0.19
NLR fine	1.15	0.22	1.79	0.24
RANS-0	0.90	−0.03	1.39	−0.16
RANS-E	0.86	−0.07	1.33	−0.22
RANS-C	0.84	−0.09	1.31	−0.24
Experiment	0.93	—	1.55	—

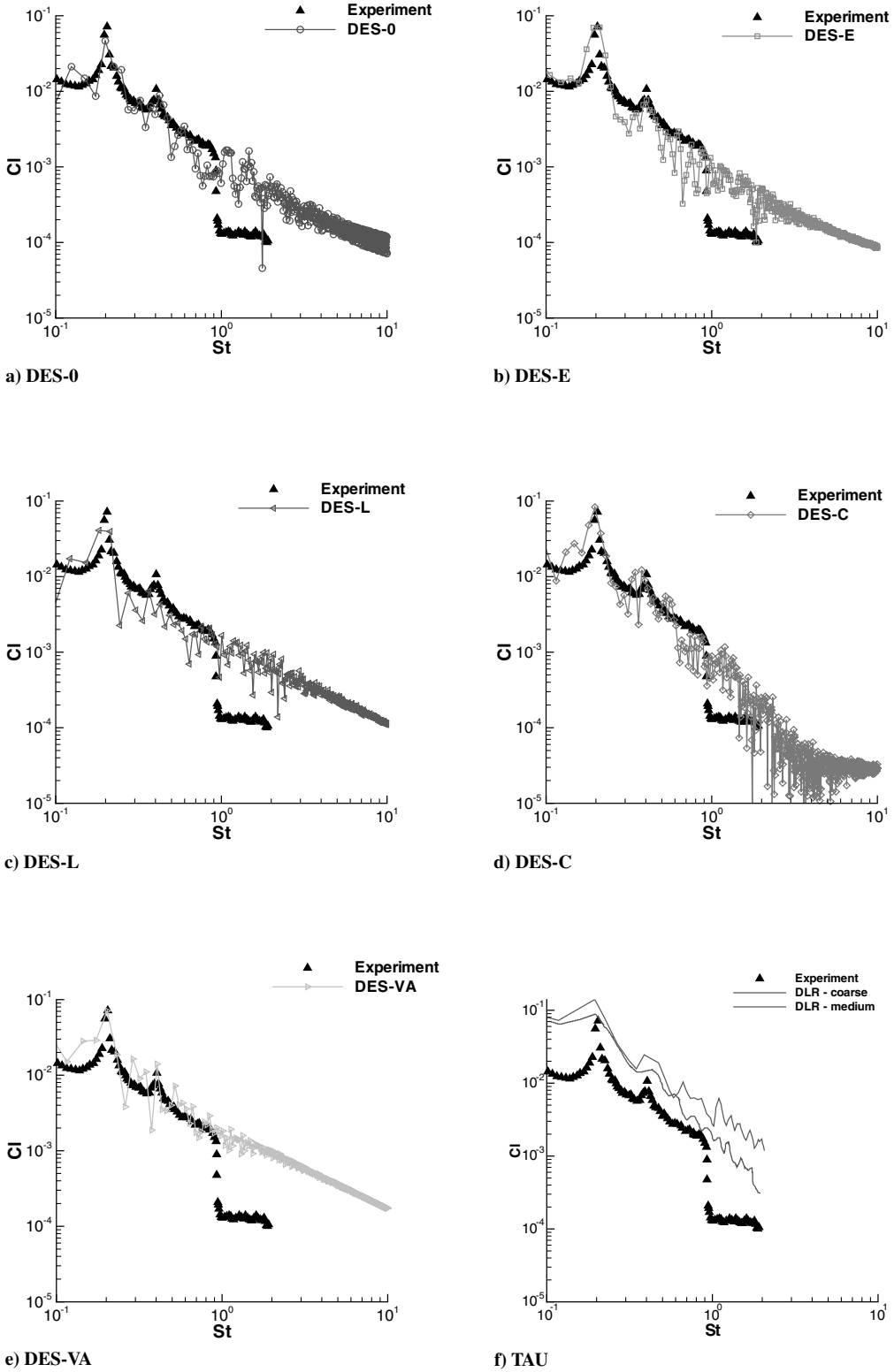

Fig. 16 Frequency content of the lift history for flow around NACA0021 airfoil at 60° AOA. Lift coefficients calculated using different DES schemes are compared: part a) DES-0; part b) DES-E; part c) DES-L; part d) DES-C; part e) DES-VA; and part f) DLR results on coarse and medium grids.

almost identical; while using DES-0 with $\alpha = 0.3$, 50% more iterations are required to reduce the flow residuals 6 orders of magnitude.

Turbulent eddies captured using DES-0, DES-E, DES-L, DES-C, and DES-VA are depicted in Figs. 18a–18e, respectively. All DES schemes capture the flow separation and vortex shedding phenomena. Turbulent small structures are resolved in all DES simulations as well.

2. RANS Results

Average pressure distribution around NACA0021 airfoil calculated using different RANS schemes are depicted in Fig. 19. DES-E results are also included for the comparison. All RANS schemes (RANS-0, RANS-E, and RANS-C) are unable to accurately capture the vortical flow physics in the separated flow region and hence overpredict the pressure distribution on the upper surface of the wing. In the attached flow region on the wing lower surface,

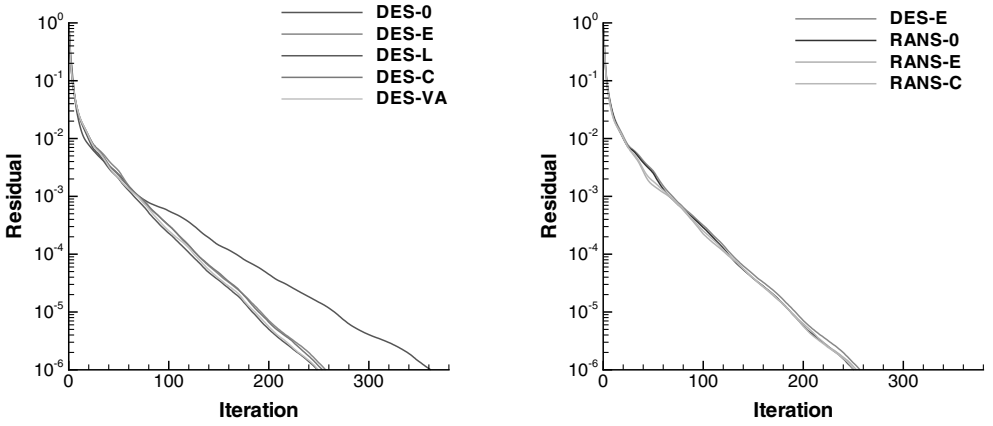

a) DES schemes b) RANS schemes

Fig. 17 Residual reduction versus GMRES iterations in a typical time step for the flow around NACA0021 airfoil at 60° AOA. Part a) DES-E0, DES-E, DES-L, DES-C, and DES-VA schemes are compared with the DES-0 with $\alpha = 0.3$; part b) RANS-E, RANS-C and DES-E schemes are compared with the baseline RANS scheme, RANS-0.

however, the accuracy of RANS schemes is comparable to what is provided by DES schemes.

The lift and drag coefficients calculated from RANS simulations are reported in Table 4. RANS schemes underpredict the lift and, more significantly, the drag coefficients. RANS-0 exhibits the best performance among all RANS schemes as its calculated average force coefficients are the closest to the experimental measurements. However, due to the issues discussed in Sec. III.D.1, no conclusive argument for the accuracy of the schemes can be made solely based on the comparison of the measured and numerically calculated force coefficients.

Spectral contents of the lift history obtained from RANS simulations are shown in Figs. 20a–20c. Here again, the first peak is accurately captured by all schemes, whereas the second peak either is significantly damped, as depicted in RANS-C predictions, or is poorly resolved due to strong spurious oscillations, as shown in RANS-E and RANS-0 results. There is some evidence that the RANS-E scheme is able to detect the spike for the second peak compared with the RANS-0 and RANS-C schemes. However, the resolution is insufficient to provide a conclusive indication.

The convergence rate of RANS-0, RANS-E, and RANS-C schemes are compared with that of the DES-E scheme in Fig. 17b. The use of different turbulence modeling has a minimal influence on the rate of the convergence in a typical time step of the unsteady flow simulation for the problems considered in this paper.

The resolution of eddies captured using RANS-0, RANS-E, and RANS-C schemes are compared in Figs. 21a–21c. The flow separation and vortex shedding from the upper surface of the wing are depicted in all RANS simulations. More three-dimensional structures are captured when the eddy-resolving algorithm or the artificial dissipation reduction via the DES-C scheme is employed, as expected.

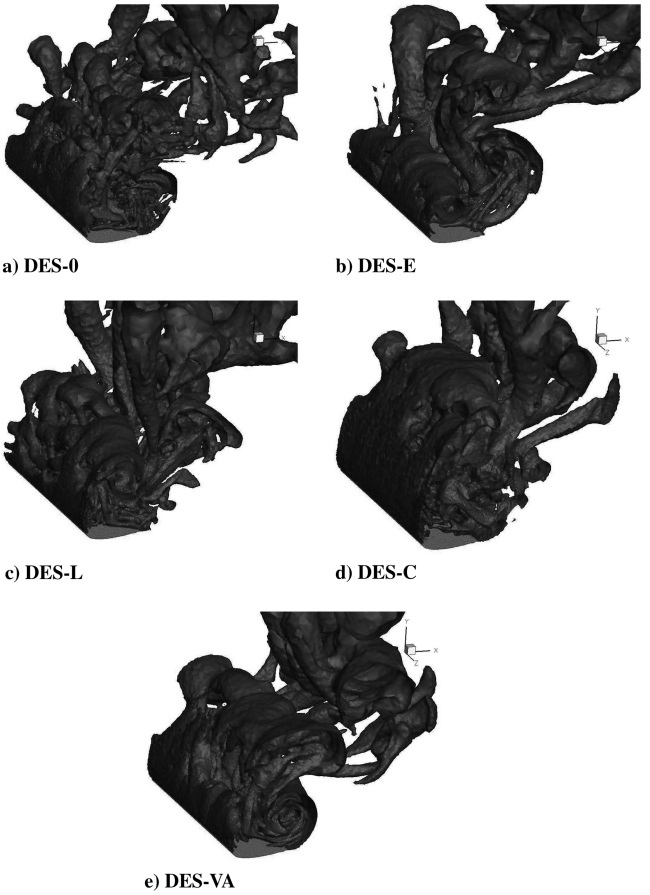

a) DES-0 b) DES-E

c) DES-L d) DES-C

e) DES-VA

Fig. 18 λ_2 isosurfaces for flow around NACA0021 airfoil at 60° AOA under static stalls condition. Flowfields calculated using DES schemes are compared: part a) DES-0; part b) DES-E; part c) DES-L; part d) DES-C; and part e) DES-VA.

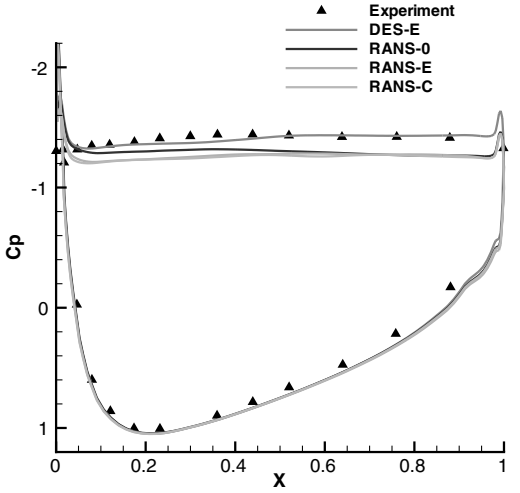

Fig. 19 Average pressure coefficient distribution around NACA0021 airfoil at $Re = 270,000$ calculated using RANS-0, RANS-E, RANS-C, and DES-E schemes.

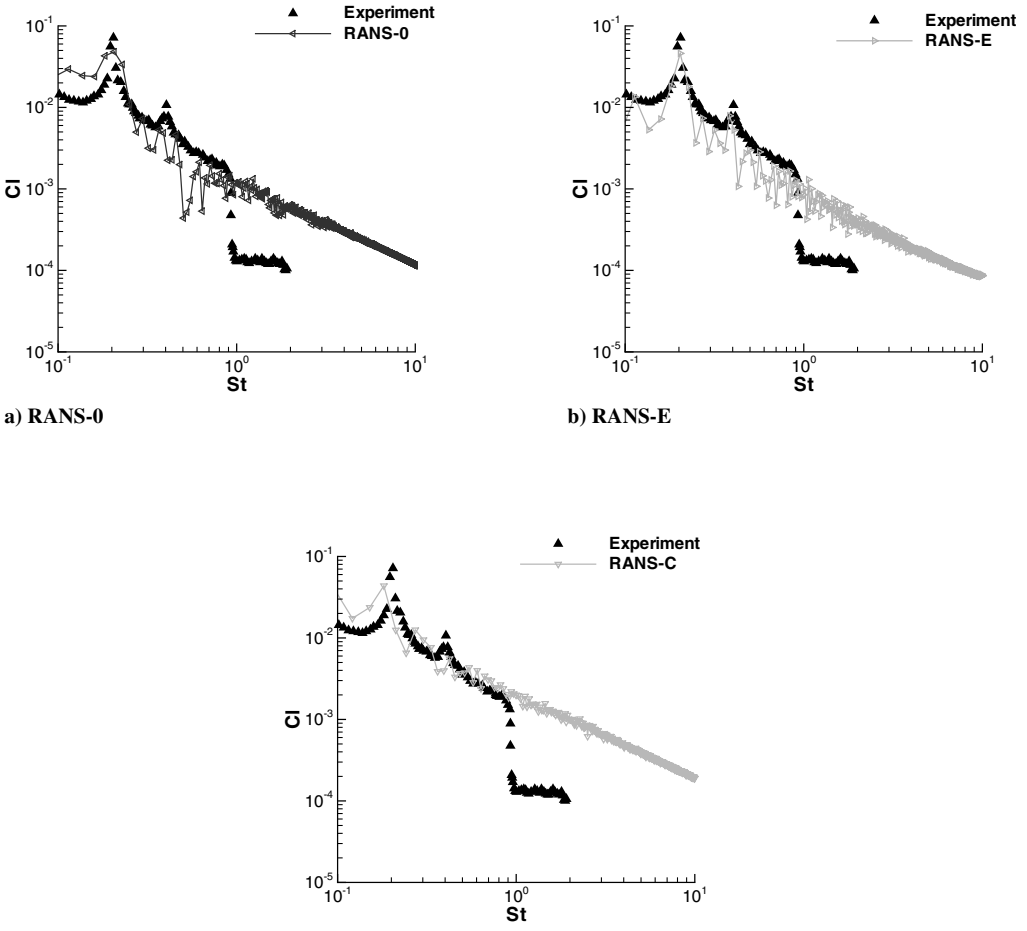

Fig. 20 Frequency content of the lift history for flow around NACA0021 airfoil at 60° AOA. Lift coefficients calculated using different RANS schemes are compared: part a) RANS-0; part b) RANS-E; and part c) RANS-C.

IV. Conclusions

A slope limiter for MUSCL schemes is proposed to reduce the overdissipation of vortices in flow simulations. The algorithm aims to preserve vortices captured in the computational domain by lowering the artificial dissipation in the vortical flow region. This is achieved via augmenting the weight of the central gradients used for the interpolation of velocity components on the swirl plane of the vortex. The performance of the algorithm to accurately capture vortex characteristics for statistically well-defined vortices and its potential as an artificial dissipation reduction scheme for turbulent flow simulations are investigated.

Once the proper spatial and temporal resolutions to capture vortices are provided, the algorithm can act to reduce the dissipation of vortices and to improve their resolution. The DIT problem emphasizes this requirement, where the resolution of proper energy spectra at the Nyquist cutoff frequency is only achieved via the DES-0 scheme.

The proposed method shows a superior performance, in comparison with standard RANS and DES schemes involving no artificial dissipation reduction treatment, in capturing tip vortex characteristics of a NACA0015 wing at high AOAs (as depicted in Figs. 6 and 10–12), as well as in resolving the second peak in spectral contents of the lift history of a NACA0021 airfoil at 60° AOA (as depicted in Fig. 16). The eddy-preserving limiter with the DES scheme provides the best resolution of the second peak in the lift coefficient spectra. This peak is not captured by the conventional van Albada limiter, and it is accompanied with significant spurious oscillations in DES-0 and DES-C results. Although an artificial dissipation scaledown algorithm with an extreme factor of 0.015 leads to a better resolution of the tip vortex in the NACA0015 test case, it requires 2.5 times more iterations to achieve the same residual reduction. Furthermore, the baseline DES method remains unstable for scaledown values smaller than 0.3. Even at this moderate value, the baseline DES' resolution of the second peak is obscured due to the presence of the spurious peaks and its convergence is 50% slower than that of the eddy-preserving algorithm.

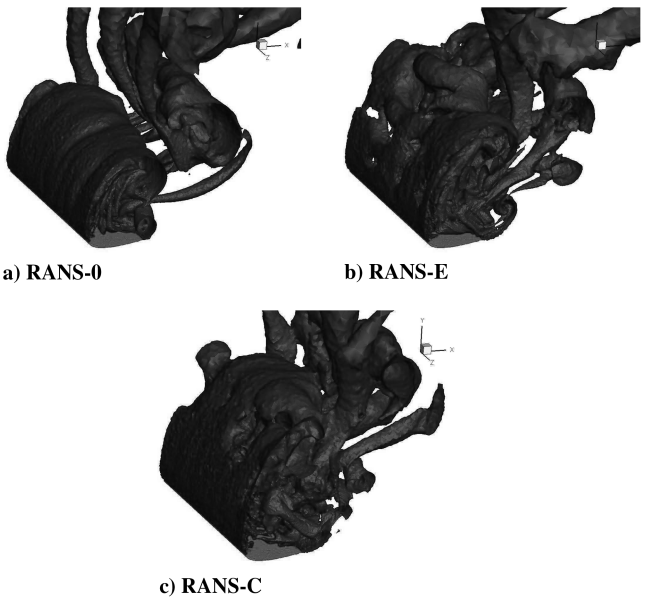

Fig. 21 λ_2 isosurfaces for flow around NACA0021 airfoil at 60° AOA under static stalls condition. Flowfields calculated using RANS schemes are compared: part a) RANS-0; part b) RANS-E; and part c) RANS-C.

The implementation of an identical slope-limiting scheme for the interpolation of other flow variables that undergo a minimum or maximum value in a vortex should be studied. In particular, a minimum pressure often exists along the axis of a free vortex. The application of a similar limiter might further enhance the vortex resolution. The behavior of the eddy-preserving limiter in the presence of shock waves and other flow discontinuities should be investigated. Additional switches for the shock detection might be necessary to turn off the eddy-preserving limiter in these regions.

Acknowledgments

Numerical simulations reported in this paper were performed on high-performance computing facilities provided by the Compute Canada and Réseau Québécois de Calcul de Haute Performance. In particular, we would like to thank the high-performance computing staves at Université de Sherbrooke, Université Laval, and Concordia University in Quebec, Canada.

The first author would like to thank the engineering staves in the Advanced Aerodynamic Department, Bombardier Aerospace in Montreal for providing a motivating environment, fruitful discussions, and feedbacks during an eight month internship program.

References

[1] Storms, B. L., and Jang, C. S., "Lift Enhancement of an Airfoil Using a Gurney Flap and Vortex Generators," *Journal of Aircraft*, Vol. 31, No. 3, 1994, pp. 542–547. doi:10.2514/3.46528

[2] Hebbar, S. K., Platzer, M. F., and Kim, C. H., "Experimental Investigation of Vortex Breakdown over a Sideslipping Canard-Configured Aircraft Model," *Journal of Aircraft*, Vol. 31, No. 4, 1994, pp. 998–1001. doi:10.2514/3.46598

[3] Soemarwoto, B. I., Boelens, O. J., Allan, M., Arthur, M. T., Bütefisch, K., Ceresola, N., and Fritz, W., "Towards the Simulation of Unsteady Manoeuvre Dominated by Vortical Flow," National Aerospace Laboratory, Technical Rept. NLR-TP-2003-397, 2003.

[4] Xing, T., Shao, J., and Stern, F., *BKW-RS-DES of Unsteady Vortical Flow for Kvlcc2 at Large Drift Angles*, Ann Arbor, MI, 2007.

[5] Dacles–Mariani, J., Zilliac, G. G., Chow, J. S., and Bradshaw, P., "Numerical/Experimental Study of a Wingtip Vortex in the Near Field," *AIAA Journal*, Vol. 33, No. 9, 1995, pp. 1561–1568. doi:10.2514/3.12826

[6] Spalart, P. R., and Shur, M., "On the Sensitization of Turbulence Models to Rotation and Curvature," *Aerospace Science and Technology*, Vol. 1, No. 5, 1997, pp. 297–302. doi:10.1016/S1270-9638(97)90051-1

[7] Brandsma, J. C., Kok, H. S., Dol, H. S., and Elsenaar, A., "Leading Edge Vortex Flow Computations and Comparison with DNW-HST Wind Tunnel Data," National Aerospace Laboratory, Technical Rept. NLR-TP-2001-238, 2001.

[8] Spalart, P. R., Jou, W. H., Strelets, M., and Allmaras, S. R., "Comments on the Feasibility of LES for Wings, and on a Hybrid RANS/LES Approach," *Advances in DNS/LES*, Greyden Press, Dayton, OH, 1997, pp. 137–147.

[9] Spalart, P. R., Deck, S., Shur, M. L., Squires, K. D., Strelets, K. Kh., and Travin, A., "A New Version of Detached-Eddy Simulation, Resistant to Ambiguous Grid Densities," *Theoretical and Computational Fluid Dynamics*, Vol. 20, No. 3, 2006, pp. 181–195. doi:10.1007/s00162-006-0015-0

[10] Jameson, A., Shmidt, W., and Turkel, E., "Numerical Solution of the Euler Equations by Finite Volume Methods Using Runge–Kutta Time Stepping Schemes," *21th AIAA Applied Aerodynamic Conference*, AIAA Paper 1981-1259, 1981.

[11] Swanson, R. C., and Turkel, E., "Multistage Schemes with Multigrid for Euler and Navier–Stokes Equations," NASA Technical Rept. 3631, 1997.

[12] Ladeinde, F., Alabi, K., Safta, C., Cai, X., and Johnson, F., *The First High-Order CFD Simulation of Aircraft: Challenges and Opportunities*, AIAA 2006-1526, 2006.

[13] Shu, C. W., "High Order Weighted Essentially Nonoscillatory Schemes for Convection Dominated Problems," *SIAM Review*, Vol. 51, No. 1, 2009, pp. 82–126. doi:10.1137/070679065

[14] Guangchu, H., Grossman, B., and Steinhoff, J., "Numerical Method for Vorticity Confinement in Compressible Flow," *AIAA Journal*, Vol. 40, No. 10, 2002, pp. 1945–1953. doi:10.2514/2.1555

[15] Steinhoff, J., "Vorticity Confinement: A New Technique for Computing Vortex Dominated Flows," *Frontiers of Computational Fluid Dynamics*, edited by D. A. Caughey and M. M. Hafez, Wiley, New York, 1994, pp. 235–263.

[16] Travin, A., Shur, M., Strelets, M., and Spalart, P. R., "Physical and Numerical Upgrades in the Detached-Eddy Simulation of Complex Turbulent Flows," *Advances in LES of Complex Flows*, Springer, New York, 2002, pp. 239–254.

[17] Ducros, F., Ferrand, V., Nicoud, F., Weber, C., Darracq, D., Gacherieu, C., and Poinsot, T., "Large-Eddy Simulation of the Shock/Turbulence Interaction," *Journal of Computational Physics*, Vol. 152, No. 2, 1999, pp. 517–549.

[18] Barone, M. F., and Roy, C. J., "Evaluation of Detached Eddy Simulation for Turbulent Wake Applications," *AIAA Journal*, Vol. 44, No. 12, 2006, pp. 3062–3071. doi:10.2514/1.22359

[19] Mohamed, K., Nadarajah, S., and Paraschivoiu, M., "Detached-Eddy Simulation of a Wing Tip Vortex at Dynamic Stall Conditions," *Journal of Aircraft*, Vol. 46, No. 4, 2009, pp. 1302–1313. doi:10.2514/1.40685

[20] Spalart, P. R., "Young-Person's Guide to Detached-Eddy Simulation Grids," NASA Technical Rept. CR-2001-211032, 2001.

[21] Löhner, R., "On Limiters for Minimal Vorticity Dissipation," *47th AIAA Aerospace Sciences Meeting*, AIAA Paper 2009-135, Jan. 2009.

[22] Chakraborty, P., Balachandar, S., and Adrian, R. J., "On the Relationships Between Local Vortex Identification Schemes," *Journal of Fluid Mechanics*, Vol. 535, No. , 2005, pp. 189–214. doi:10.1017/S0022112005004726

[23] Hallo, L., Le Ribault, C., and Buffat, M., "Implicit Mixed Finite Volume-Finite Element Method for Solving 3D Turbulent Compressible Flows," *International Journal for Numerical Methods in Fluids*, Vol. 25, No. 11, 1997, pp. 1241–1261. doi:10.1002/(SICI)1097-0363(19971215)25:11<1241::AID-FLD595>3.0.CO;2-1

[24] Turkel, E., Vatsa, V. N., and Radespiel, R., "Preconditioning Methods for Low-Speed Flows," Technical Rept. TR-96-57, Oct. 1996,

[25] Viozat, C., "Implicit Upwind Schemes for Low Mach Number Compressible Flows," INRIA, Rept. 3084, Jan. 1997.

[26] Turkel, E., "Robust Low Speed Preconditioning for Viscous High Lift Flows," *40th AIAA Aerospace Science Meeting and Exhibit*, AIAA, Paper 2002-962, Jan. 2002.

[27] Sarkis, M., and Koobus, B., "A Scaled and Minimum Overlap Restricted Additive Schwarz Method with Application to Aerodynamics," *Computer Methods in Applied Mechanics and Engineering*, Vol. 184, Nos. 2–4, 2000, pp. 391–400. doi:10.1016/S0045-7825(99)00236-4

[28] Saad, Y., *Iterative Methods for Sparse Linear Systems*, 2nd ed., SIAM, Philadelphia, 2003.

[29] Turkel, E., and Vatsa, V. N., "Local Preconditioners for Steady and Unsteady Flow Applications," *Mathematical Modelling and Numerical Analysis*, Vol. 39, No. 3, 2005, pp. 515–535. doi:10.1051/m2an:2005021

[30] Spalart, P. R., and Allmaras, S. R., "One-Equation Turbulence Model for Aerodynamic Flows," *Recherche Aerospatiale*, Vol. 1, No. 1, 1994, pp. 5–21.

[31] Bunge, U., Mockett, C., and Thiele, F., "Guidelines for Implementing Detached-Eddy Simulation Using Different Models," *Aerospace Science and Technology*, Vol. 11, No. 5, 2007, pp. 376–385. doi:10.1016/j.ast.2007.02.001

[32] Jiminez, J., "A Selection of Test Cases for the Validation of Large-Eddy Simulations of Turbulent Flows," AGARD Technical Rept. No. 345.

[33] van Leer, B., "Upwind-Difference Methods for Aerodynamics Problems Governed by the Euler Equations," *Lectures in applied mathematics*, Vol. 22, No. 2, 1985, pp. 327–336.

[34] Jeong, J., and Hussain, F., "On the Identification of a Vortex," *Journal of Fluid Mechanics*, Vol. 285, No. 1, 2006, pp. 69–94. doi:10.1017/S0022112095000462

[35] Chong, M. S., Perry, A. E., and Cantwell, B. J., "A General Classification of Three-Dimensional Flow Fields," *Physics of Fluids A*, Vol. 2, No. 5, 1990, pp. 765–777. doi:10.1063/1.857730

[36] Zhou, J., Adrian, R. J., Balachandar, S., and Kendall, T. M., "Mechanisms for Generating Coherent Packets of Hairpin Vortices," *Journal of Fluid Mechanics*, Vol. 387, No. , 1999, pp. 353–396. doi:10.1017/S002211209900467X

[37] Dervieux, A., and Desideri, J. A., "Compressible Flow Solvers Using Unstructured Grids," Technical Rept. INRIA-RR-1732, INRIA, 1992.

[38] Birch, D., and Lee, T., "Tip Vortex Behind a Wing Undergoing Deep-Stall Oscillation," *AIAA Journal*, Vol. 43, No. 10, 2005, pp. 2081–2092. doi:10.2514/1.13139

[39] Birch, D., and Lee, T., "Investigation of the Near-Field Tip Vortex Behind an Oscillating Wing," *Journal of Fluid Mechanics*, Vol. 544, No. 1, 2005, pp. 201–241. doi:10.1017/S0022112005006804

[40] Weinman, K., Knopp, T., Mockett, C., Bunge, U., Thiele, F., van der Ven, H., and Kok, J. C., "A Grid Convergence Study for DES-Like Simulations of a Stalled Airfoil," DESider Workshop, Stockholm, 2005.

[41] Swalwell, K. E., Sheridan, J., and Melbourne, W. H., "Frequency Analysis of Surface Pressures on an Airfoil After Stall," *21th AIAA Applied Aerodynamic Conference*, AIAA Paper 2003-3416, June 2009.

[42] Haase, W., Braza, M., and Revell, A. (eds.), *DESider: A European Effort on Hybrid RANS-LES Modelling: Results of the European-Union Funded Project 2004–2007*, 1st ed., Springer–Verlarg, Berlin, 2009.

Z. Wang
Associate Editor